Numerical Micromagnetics : Finite Difference Methods

J. Miltat[1] and M. Donahue[2]

[1] Laboratoire de Physique des Solides,
Université Paris XI Orsay & CNRS, 91405 Orsay, France
miltat@lps.u-psud.fr

[2] Mathematical & Computational Sciences Division,
National Institute of Standards and Technology, Gaithersburg MD 20899-8910,
USA
michael.donahue@nist.gov

Summary. Micromagnetics is based on the one hand on a continuum approximation of exchange interactions, including boundary conditions, on the other hand on Maxwell equations in the non-propagative (static) limit for the evaluation of the demagnetizing field. The micromagnetic energy is most often restricted to the sum of the exchange, demagnetizing or (self-)magnetostatic, Zeeman and anisotropy energies. When supplemented with a time evolution equation, including field induced magnetization precession, damping and possibly additional torque sources, micromagnetics allows for a precise description of magnetization distributions within finite bodies both in space and time. Analytical solutions are, however, rarely available. Numerical micromagnetics enables the exploration of complexity in small size magnetic bodies. Finite difference methods are here applied to numerical micromagnetics in two variants for the description of both exchange interactions/boundary conditions and demagnetizing field evaluation. Accuracy in the time domain is also discussed and a simple tool provided in order to monitor time integration accuracy. A specific example involving large angle precession, domain wall motion as well as vortex/antivortex creation and annihilation allows for a fine comparison between two discretization schemes with as a net result, the necessity for mesh sizes well below the exchange length in order to reach adequate convergence.

The first two-dimensional numerical simulation of a domain wall structure was published in 1969. In his celebrated work, A. E. LaBonte [1], showed that the structure of a domain wall in an infinite magnetically soft thin film with thickness in the 100 nm range was neither Bloch- nor Néel-type, but somehow a mixture of both. Some 35 years later, numerical micromagnetics has become

ubiquitous and rather unavoidable a tool in the study of magnetic nanostructures. Rather unexpectedly, LaBonte's pioneering work remains modern due to the immense progress made in the elaboration and observation of magnetic nanostructures. Suffice it to say that three-dimensional numerical micromagnetics unravels much hidden complexity and yet firm underlying logics in the wall structures and magnetization distribution within faceted Iron nanocrystals, in agreement with the most demanding experiments [2]. The present chapter deals with numerical micromagnetics using finite difference methods and is organized as follows. Section 1 captures the essentials of micromagnetics, a continuum theory of ferro- or ferrimagnetic bodies, and thus provides the necessary background for the understanding of the following sections. Sections 2 and 3 are devoted to numerical implementations of the micromagnetic continuum theory with primacy given to the field acting on the magnetization and energy, respectively. Section 4 addresses the issue of accuracy in the time domain. Lastly, based on a single but demanding example, a brief comparison between the two approaches is attempted in Section 5.

1 Background

If solely referring to the number of lattice sites in a micron-size magnetic element with thickness in the few nm range, it becomes immediately clear that fully ab-initio methods aimed at defining the local value of the magnetic moment and its direction are out of reach. Micromagnetics is a continuum theory of ferro or ferrimagnetic materials, which allows for the computation of magnetization distributions in samples of arbitrary shape [3, 5, 6]. Its basic assumptions consist in considering the magnetization modulus to remain constant ($\mathbf{M} = M_{\mathrm{s}}\mathbf{m}$, $\mathbf{m} \cdot \mathbf{m} = 1$) and all vector quantities (the magnetization $\mathbf{M}$, the exchange $\mathbf{H}_{\mathrm{Exch}}$ and demagnetizing fields $\mathbf{H}_{\mathrm{d}}$, especially) to vary slowly at the atomic scale. The components of $\mathbf{m}$ are the direction cosines of the magnetization $\mathbf{M}$. Micromagnetics is based on the one hand on the notion of an effective field acting on the magnetization [3, 4, 5, 6, 7], on the other hand on an equation depicting magnetization dynamics known as the Landau-Lifshitz or Landau-Lifshitz-Gilbert (LLG) equation, depending on the exact formulation of damping. According to Brown's theory [3], the effective field is the functional derivative of the energy density ε, w.r.t. magnetization:

$$\mathbf{H}_{\mathrm{eff}} = -\frac{1}{\mu_0 M_{\mathrm{s}}}\frac{\delta\varepsilon}{\delta\mathbf{m}} \quad . \tag{1}$$

As shown earlier in this volume [8], the effective field usually contains contributions stemming from the exchange, anisotropy, applied field or Zeeman and demagnetizing energy densities, namely

$$\mathbf{H}_{\mathrm{eff}} = -\frac{1}{\mu_0 M_{\mathrm{s}}}\frac{\delta\varepsilon}{\delta\mathbf{m}} = \frac{2A}{\mu_0 M_{\mathrm{s}}}\nabla^2\mathbf{m} - \frac{1}{\mu_0 M_{\mathrm{s}}}\frac{\delta\varepsilon_{\mathrm{K}}}{\delta\mathbf{m}} + \mathbf{H}_{\mathrm{app}} + \mathbf{H}_{\mathrm{d}} \quad , \tag{2}$$

corresponding to the following micromagnetic energy:

$$E = \int_V \left[A \left(\boldsymbol{\nabla} \mathbf{m} \right)^2 + \varepsilon_k - \mu_0 M_s \left(\mathbf{H}_{\text{app}} \cdot \mathbf{m} \right) - \frac{1}{2} \mu_0 M_s \left(\mathbf{H}_d \cdot \mathbf{m} \right) \right] d^3 r \quad , \tag{3}$$

where, A is the exchange constant (units J/m), ϵ_K the anisotropy energy density (units J/m^3), $\mathbf{H}_{\text{app}}$ and $\mathbf{H}_d$ the applied and demagnetizing field (units A/m), respectively. As noted as early as 1949 by C. Kittel [9], the exchange energy may, by combining the constraint $\mathbf{m}^2 = 1$ with the vector relation $|\nabla f|^2 = \nabla \cdot (f \nabla f) - f \nabla^2 f$, be expressed in either of the following forms:

$$E_{\text{exch}} = \int_V \left[A \left(\boldsymbol{\nabla} \mathbf{m} \right)^2 \right] d^3 r = - \int_V \left[A \mathbf{m} \cdot \left(\frac{\partial^2 \mathbf{m}}{\partial x^2} + \frac{\partial^2 \mathbf{m}}{\partial y^2} + \frac{\partial^2 \mathbf{m}}{\partial z^2} \right) \right] d^3 r \quad . \tag{4}$$

Additional energy terms may be included in the energy, e.g. terms arising from magnetostriction, or longer range exchange coupling across nonmagnetic spacer layers in spin valves [10, 11]; such terms will not be considered below.

When considering an energy density functional solely implying exchange and magnetostatic interactions (the ideally soft magnetic material limit), dimensional arguments soon lead to the definition of a characteristic length known as the (magnetostatic-) exchange length

$$\Lambda = \sqrt{\frac{2A}{\mu_0 M_s^2}} \quad , \tag{5}$$

a quantity labeled l_s in [8]. The exchange length rarely exceeds a few nanometers in 3d ferromagnetic materials or their alloys, thereby imposing severe constraints on the mesh size in numerical simulations.

The effective field (see Eq.(2)) exerts a torque on the magnetization that is proportional to $\mathbf{M} \times \mathbf{H}$. In full analogy with classical mechanics, the rate of change of the magnetization -angular momentum- is, in the absence of damping, equal to the torque, namely

$$\frac{d}{dt} \mathbf{m}(t) = -\gamma_0 \left[\mathbf{m}(t) \times \mathbf{H}_{\text{eff}}(t) \right] \quad . \tag{6}$$

It follows from (6) that as long as the torque is zero, the angular momentum is conserved. For a free electron, γ_0 is equal to $\approx 2.21 \times 10^5 \, (\text{A/m})^{-1} \, \text{s}^{-1}$. Still in the absence of damping, magnetization motion reduces to a precession of the magnetization around the effective field, with frequency:

$$\omega_0 = \gamma_0 H_{\text{eff}} \quad , \tag{7}$$

i.e. $\approx 28 \, \text{MHz/mT}$ in units of $\mu_0 H_{\text{eff}}$ for a free electron spin.

Gilbert damping [12] is most simply introduced if adding to the effective field an Ohmic type dissipation term, namely

$$\mathbf{H}_{\text{eff}} = \mathbf{H}_{\text{eff}} - \alpha \frac{1}{\gamma_0 M_{\text{s}}} \frac{d\mathbf{M}}{dt} \quad , \tag{8}$$

where, α is the (dimensionless) Gilbert damping parameter. Introducing (8) into (6) leads to the so-called LLG equation,

$$\frac{d\mathbf{m}}{dt} = -\gamma_0 \left(\mathbf{m} \times \mathbf{H}_{\text{eff}} \right) + \alpha \left[\mathbf{m} \times \frac{d\mathbf{m}}{dt} \right] \quad , \tag{9}$$

or its numerically more tractable and mathematically equivalent form

$$\left(1 + \alpha^2 \right) \frac{d\mathbf{m}}{dt} = -\gamma_0 \left[\mathbf{m} \times \mathbf{H}_{\text{eff}} + \alpha \left[\mathbf{m} \times \left(\mathbf{m} \times \mathbf{H}_{\text{eff}} \right) \right] \right] \quad , \tag{10}$$

Given a magnetization distribution $\mathbf{m(r, t)} = \mathbf{M(r, t)}/M_{\text{s}}$, the LLG equation specifies the magnetization distribution at time $t+dt$ provided due respect of boundary conditions is maintained. Alternatively, if a sole magnetization distribution at equilibrium is sought for, the only condition that needs to be satisfied reads:

$$\mathbf{m} \times \mathbf{H}_{\text{eff}} = \mathbf{0} \tag{11}$$

Because the exchange energy involves the square of the gradient of the magnetization components, its variation gives rise not only to the exchange contribution to the effective field in (2) but also to boundary conditions. Boundary conditions (BC's) that arise from the sole symmetry breaking of exchange interactions at surfaces are referred to as "free" BC's. Their mathematical expression in the continuum limit reads:

$$\text{A} \left(\mathbf{m} \times \frac{\partial \mathbf{m}}{\partial \mathbf{n}} \right) = 0 \quad , \tag{12}$$

which is equivalent to the Neumann boundary condition

$$\frac{\partial \mathbf{m}}{\partial \mathbf{n}} = 0 \tag{13}$$

since $\mathbf{m}^2 = 1$. In the presence of surface anisotropy, energy density

$$\varepsilon_{\text{K}_{\text{S}}} = \text{K}_{\text{s}} \left(1 - (\mathbf{n} \cdot \mathbf{m})^2 \right) \quad , \tag{14}$$

and interlayer exchange, energy density

$$\varepsilon_{\text{J}} = \text{J}_1 \left(1 - \mathbf{m} \cdot \mathbf{m}' \right) + \text{J}_2 \left(1 - (\mathbf{m} \cdot \mathbf{m}')^2) \right) \quad , \tag{15}$$

where $\mathbf{m}'$ defines the exchange-bias direction at the interface with the ferro- or ferrimagnetic body, boundary conditions may be expressed [13] either as

$$2A \left(\mathbf{m} \times \frac{\partial \mathbf{m}}{\partial \mathbf{n}} \right) - 2K_S \left(\mathbf{m} \cdot \mathbf{n} \right) \left(\mathbf{m} \times \mathbf{n} \right)$$

$$- J_1 \left(\mathbf{m} \times \mathbf{m}' \right) - 2J_2 \left(\mathbf{m} - \mathbf{m}' \right) \left(\mathbf{m} \times \mathbf{m}' \right) = 0 \quad , \quad (16)$$

or,

$$\frac{\partial \mathbf{m}}{\partial \mathbf{n}} = \frac{K_S}{A} \left(\mathbf{m} \cdot \mathbf{n} \right) \left(\mathbf{n} - \left(\mathbf{m} \cdot \mathbf{n} \right) \mathbf{m} \right)$$

$$- \left(\frac{J_1}{2A} + \frac{J_2}{A} \left(\mathbf{m} \cdot \mathbf{m}' \right) \right) \left(\left(\mathbf{m} \cdot \mathbf{m}' \right) \mathbf{m} - \mathbf{m}' \right) \quad . \quad (17)$$

See also references [3, 14, 15].

Altogether, as long as the exchange parameter A is independent of position $\mathbf{r}$, a magnetization continuum owing to micromagnetics is at zero temperature governed by the set of equations:

$$\mathbf{m} = \mathbf{m} \left(\mathbf{r}, t \right)$$
$$\mathbf{H}_{\text{eff}} = \mathbf{H}_{\text{eff}} (\mathbf{r}, t)$$
$$\mathbf{H}_{\text{d}} = \mathbf{H}_{\text{d}} (\mathbf{r}, t)$$
$$\mathbf{H}_{\text{eff}} = \frac{2A}{\mu_0 M_{\text{s}}} \nabla^2 \mathbf{m} + \mathbf{H}_{\text{app}} + \mathbf{H}_{\text{d}} - \frac{1}{\mu_0 M_{\text{s}}} \frac{\delta \varepsilon_{\text{k}}}{\delta \mathbf{m}}$$
$$\frac{\partial \mathbf{m}}{\partial \mathbf{n}} = \frac{K_S}{A} \left(\mathbf{m} \cdot \mathbf{n} \right) \left[\mathbf{n} - \left(\mathbf{m} \cdot \mathbf{n} \right) \mathbf{m} \right] - \left[\frac{J_1}{2A} + \frac{J_2}{A} \left(\mathbf{m} \cdot \mathbf{m}' \right) \right] \left[\left(\mathbf{m} \cdot \mathbf{m}' \right) \mathbf{m} - \mathbf{m}' \right] \quad ,$$

$$(18)$$

augmented with the LLG equation of magnetization motion (9) or the equilibrium condition (11).

In case the exchange constant would be position dependent, an additional term would appear in the exchange components of the effective field. In the following, the exchange constant is assumed to remain constant, i.e. a sole function of the ferro- or ferrimagnetic material composition. It has also been implicitly assumed that the system under study was free of surface-specific damping. On the other hand, the saturation magnetization, the anisotropy as well as the damping constant may be modulated according to position without introducing modifications in the set of equations (18).

This chapter considers the finite difference approach to solving these equations, where the magnetization is sampled on a uniform rectangular mesh at points $(x_0 + i \Delta_x, y_0 + j \Delta_y, z_0 + k \Delta_z)$. The computational cell is centered about the sample point with dimensions $\Delta_x \times \Delta_y \times \Delta_z$. The main advantages of the finite difference approach are ease of implementation, simplicity of meshing, efficient evaluation of the demagnetizing energy (via, e.g., Fast Fourier Transform (FFT) methods), and the accessibility of higher order methods. A main disadvantage of this approach is that sampling curved boundaries with a rectangular mesh results in a "staircase" type approximation to the geometry,

which can produce significant errors in the computation. Corrections for this artifact are possible [16, 17, 18], but are not discussed in the present text. The next two sections present two approaches to the problem of discretizing the continuous equations discussed above. The first, Sec. 2, treats (2) as fundamental, and focuses primarily on computing an accurate value of $\mathbf{H}_{\text{eff}}$ directly from $\mathbf{m}$. We call this the field-based approach. The alternative energy-based approach, presented in Sec. 3, is directed first at computing the micromagnetic energy (3). The effective field $\mathbf{H}_{\text{eff}}$, which is needed in the LLG equation (9), is computed from the energy via the discrete analog of (1). The $\mathbf{H}_{\text{eff}}$ computed in this manner is the field value averaged across the corresponding discretization cell. Results using the two methods on a sample problem are compared in Sec. 5.

2 Finite difference micromagnetics: field-based approach

As stated above, in a field-based approach [13, 19, 20], one is seeking a numerical solution to the LLG equation (18) based on a direct evaluation of the effective field components under the constraint of problem specific boundary conditions. In this approach, the energy (density) plays a role only to the extent that the effective field is the gradient of the former.

Looking at (18) immediately reveals that a number of derivatives will require evaluation, namely first and second-order derivatives of the magnetization components in order to define the divergence of the magnetization ($\boldsymbol{\nabla} \cdot \mathbf{m}$) and the components of the exchange field ($\nabla^2 \mathbf{m}$), respectively. The magnetization components along boundaries also need to be evaluated in order to define surface charges ($\mathbf{m} \cdot \mathbf{n}$) that do contribute to the demagnetizing field. Boundary conditions need to be incorporated in the evaluation of the effective field without loss of accuracy. Finally, solution of the LLG equation does require both stability and accuracy. This paragraph is organized as follows: in a first step we describe the various steps to be taken in order to provide a numerical estimate of the demagnetizing field. In the next step, starting with an evaluation of the exchange field in the bulk, it is first shown how boundary conditions may be included without too heavy a cost in accuracy, at least for so-called free boundary conditions. The third step explains how general boundary conditions may be introduced. Because the problem of an accurate solution of the LLG equation is common to both the field-based and energy-based finite difference methods, it is treated separately (see section 3)

2.1 Demagnetizing field evaluation

For a magnetization continuum, the demagnetizing field, in full similarity to electrostatics, arises from volume and surface charges

$$\begin{aligned}
\lambda_{\text{V}} &= -\mu_0 M_{\text{s}} \left(\boldsymbol{\nabla} \cdot \mathbf{m} \right) , && \text{in the volume} \quad , \\
\sigma_{\text{S}} &= +\mu_0 M_{\text{s}} \left(\mathbf{m} \cdot \mathbf{n} \right) , && \text{at free surfaces} \quad ,
\end{aligned} \tag{19}$$

and derives from the scalar potential expressed as follows

$$\mathbf{H}_\mathrm{d}(\mathbf{r}) = -\boldsymbol{\nabla}\varPhi_\mathrm{d}(\mathbf{r}) \quad,$$
$$\varPhi_\mathrm{d}(\mathbf{r}) = \frac{1}{4\pi\mu_0} \left[\int_V \frac{\lambda_\mathrm{V}(\mathbf{r}')}{|\mathbf{r} - \mathbf{r}'|}\, d^3\mathbf{r}' + \int_S \frac{\sigma_\mathrm{S}(\mathbf{r}')}{|\mathbf{r} - \mathbf{r}'|}\, d^2\mathbf{r}' \right] \quad. \tag{20}$$

Figure 1 illustrates the geometrical relations between vectors entering (20).

It follows from 19 and 20 that the demagnetizing field may be directly expressed as

$$\mathbf{H}_\mathrm{d}(\mathbf{r}) = \frac{1}{4\pi\mu_0} \left[\int_V \frac{(\mathbf{r} - \mathbf{r}')\,\lambda_\mathrm{V}(\mathbf{r}')}{|\mathbf{r} - \mathbf{r}'|^3}\, d^3\mathbf{r}' + \int_S \frac{(\mathbf{r} - \mathbf{r}')\,\sigma_\mathrm{S}(\mathbf{r}')}{|\mathbf{r} - \mathbf{r}'|^3}\, d^2\mathbf{r}' \right] \quad. \tag{21}$$

To the existence of a demagnetizing field corresponds a magnetostatic energy density functional

$$\varepsilon_\mathrm{demag} = -\frac{1}{2}\mu_0\left(\mathbf{H}_\mathrm{d} \cdot \mathbf{M}\right) = -\frac{1}{2}\mu_0 M_\mathrm{s}\left(\mathbf{H}_\mathrm{d} \cdot \mathbf{m}\right) \quad, \tag{22}$$

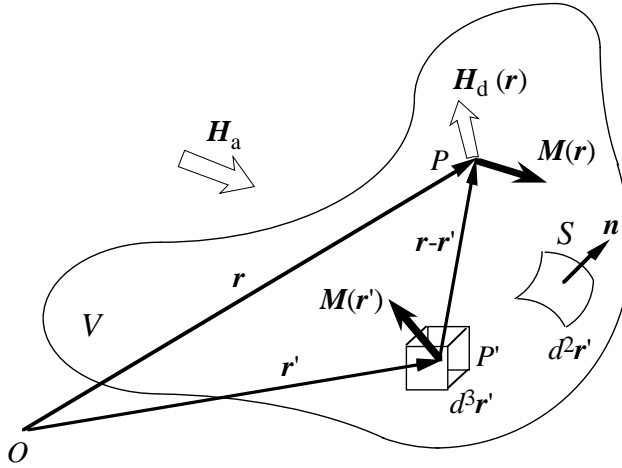where the $1/2$ prefactor stems from the fact that $\mathbf{M}$ is the source of $\mathbf{H}_\mathrm{d}$.

Fig. 1. Geometry attached to (20).

Four remarks ought to be made here. First, charges must sum up to zero because of the fundamentally dipolar nature of magnetism. Second, contrary to the Zeeman contribution to the total energy, the magnetostatic energy, obtained through summation over the volume and external surface of the element of the energy density (22), is necessarily positive or nil. It follows that, in a soft magnetic material, where the magnetostatic energy becomes the leading term, energy may only be minimized by the pole avoidance principle.

This means that, whenever possible, the magnetization will tend to be parallel to external boundaries and adopt configurations satisfying $\boldsymbol{\nabla} \cdot \mathbf{m} = 0$ in the volume. Clearly, this may only be achieved at the expense of exchange energy as well as anisotropy energy when present. Third, because of the long range decay of magnetostatic interactions, large errors are inevitably made when truncation of the integrals is attempted. Last, but not least, one easily recognizes in the integrals of (20) a convolution product. Therefore, from a numerical point of view, much of the computation load may be relieved via an extensive use of Fast Fourier Transforms (FFT's).

Decomposing the magnetic volume into cells (index i',j',k') with <u>constant</u> magnetization divergence and the outer surface into tiles (index l',m',n') with <u>constant</u> charge density (see Fig 2) immediately leads to an easy and yet accurate numerical estimate of the demagnetizing field at location $\mathbf{r}$. Eq. (21) then reduces to a finite sum, namely,

$$\mathbf{H}_{\mathrm{d}}(\mathbf{r}) = \frac{1}{4\pi\mu_0} \sum_{i',j',k'} \left[\lambda_{\mathrm{V}}(i',j',k') \int_{V'(i',j',k')} \frac{(\mathbf{r} - \mathbf{r}')}{|\mathbf{r} - \mathbf{r}'|^3} \, d^3\mathbf{r}' \right]$$
$$+ \frac{1}{4\pi\mu_0} \sum_{l',m',n'} \left[\sigma_{\mathrm{S}}(l',m',n') \int_{S'(l',m',n')} \frac{(\mathbf{r} - \mathbf{r}')}{|\mathbf{r} - \mathbf{r}'|^3} \, d^2\mathbf{r}' \right] \quad , \quad (23)$$

where $\mathbf{r}'$ now spans either the volume of cell i',j',k' or the area of tile l',m',n'. The integrals in Eq. (23) therefore reduce to purely geometrical coefficients that only need to be computed once. Eq. (23) may thus be rewritten as:

$$\mathbf{H}_{\mathrm{d}}(\mathbf{r}) = \frac{1}{4\pi\mu_0} \sum_{i',j',k'} \lambda_{\mathrm{V}}(i',j',k') \, C_{\mathrm{V}}(\mathbf{r},i',j',k')$$
$$+ \frac{1}{4\pi\mu_0} \sum_{l',m',n'} \sigma_{\mathrm{S}}(l',m',n') \, C_{\mathrm{S}}(\mathbf{r},l',m',n') \quad . \quad (24)$$

Note that such a decomposition is achieved if assuming the magnetization to be a trilinear function of the coordinates x,y,z within the magnetic volume whilst being constant over the area of a tile. All interaction coefficients C_{V} and C_{S} are definite integrals with kernels $\frac{x-x'}{|\mathbf{r}-\mathbf{r}'|^3}$, $\frac{y-y'}{|\mathbf{r}-\mathbf{r}'|^3}$, $\frac{z-z'}{|\mathbf{r}-\mathbf{r}'|^3}$ for the x, y and z demagnetizing field components, respectively. For instance, the x component of the demagnetizing field arising from a volume cell is given by Eq. (24) with

$$C_{\mathrm{V}}^x = \int_{x_1'}^{x_2'} \int_{y_1'}^{y_2'} \int_{z_1'}^{z_2'} \frac{x - x'}{|\mathbf{r} - \mathbf{r}'|^3} dx' dy' dz' \quad . \tag{25}$$
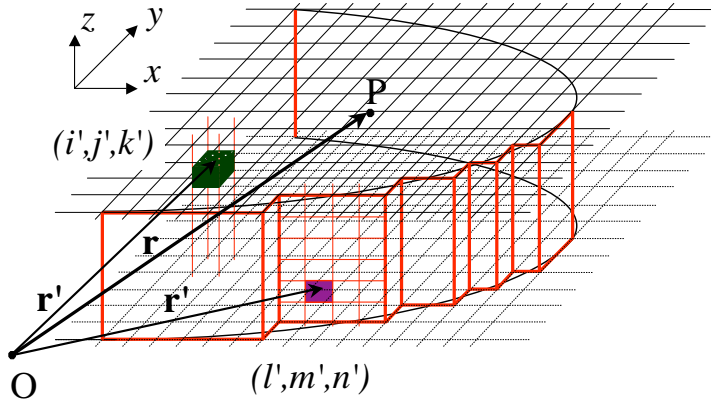
Fig. 2. The demagnetizing field at point P(**r**) is built-up from contributions arising from volume cells with constant magnetization divergence and surface tiles with constant charge density. In this drawing, the physical frontier consists in the top and bottom planes, and the continuous rim boundary (in black). The numerical rim boundary is stair-case like (in red).

Similarly, the z component of the demagnetizing field arising from a tile parallel to the xy plane is given by Eq. (24) with

$$C_{\mathrm{Sxy}}^z = \int\limits_{x_1'}^{x_2'} \int\limits_{y_1'}^{y_2'} \frac{z - z'}{|\mathbf{r} - \mathbf{r}'|^3} dx' dy' \quad . \tag{26}$$

For parallelepipedic volume cells and rectangular surface tiles, all interaction coefficients may be evaluated with the help of the integrals listed in Appendix A. H^{111} integrals apply to constant divergence volume cells whereas H^{110}, H^{011} and H^{101} integrals apply to tiles parallel to the xy, yz and xz planes, respectively.

Lastly, for both a regular meshing and a regular sampling of the field (volume cells centers or apices seem natural choices), translational invariance of the interaction coefficients allows for the use of Fast Fourier Transforms in the evaluation of the demagnetizing field [21, 22, 23, 24, 25]. FFT's considerably reduce the computational load in numerical micromagnetics. Because, however, the magnetization distribution is not usually periodic, zero-padding techniques need to be implemented [26]. Further discussion on the use of FFT's in numerical micromagnetics is deferred to section 3.4. We note in closing this section that a direct evaluation of the field at the apices of the volume cells leads to weak divergences of the demagnetizing field [27]. It has been shown both numerically [28] and analytically [29] that the log-type divergence of the demagnetizing field along the edges and at the apices of a uniformly magnetized parallelepiped are balanced *via* tiny rotations of the magnetization close

to boundaries that take place over distances smaller than the exchange length. Methods relying on the direct evaluation of the demagnetizing field therefore practically restrict the choice of the field sampling points to cells centers.

2.2 Derivatives evaluation

Consider a regular, differentiable one-dimensional scalar function $f(x)$ sampled at regular intervals, a (see Fig. 3-a). Second order Taylor expansion readily yields expressions for the first and second central derivatives that are widely used in numerics, namely $\frac{df}{dx} = \frac{f_{i+1}-f_{i-1}}{2a}$ and $\frac{d^2 f}{dx^2} = \frac{f_{i+1}-2f_i+f_{i-1}}{a^2}$, respectively.
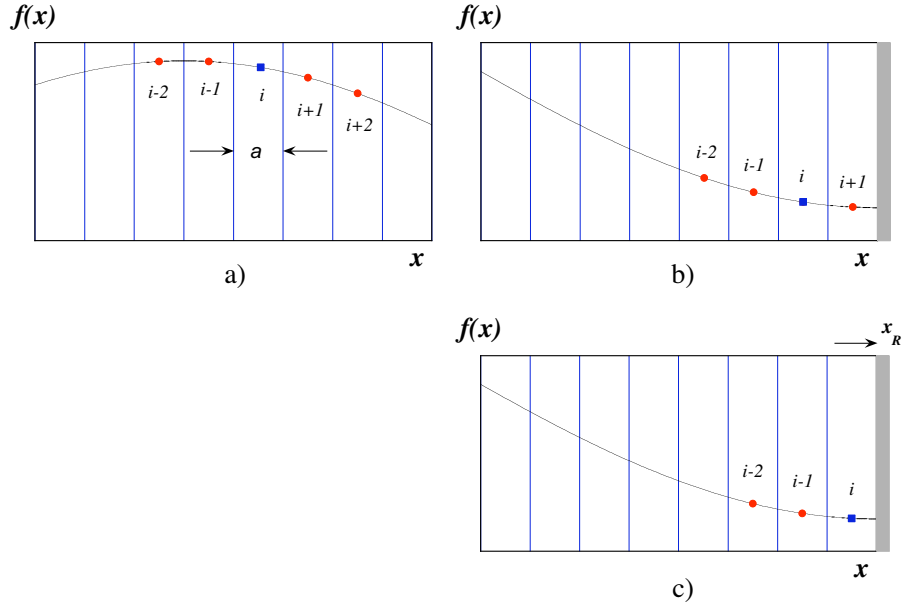
Fig. 3. Mesh geometry (**a**) Function of the sole scalar x. (**b**) Mesh points second to closest to boundary. (**c**) Mesh points closest to boundary.

However, the numerical derivation of the structure of a simple Bloch wall using such expressions soon reveals that second order Taylor expansion leads to restricted accuracy. Fourth order expansion has actually been found to prove much superior [30, 31, 24, 13]. Taylor expansion of function $f(x)$ around $x = x_i$ reads :

$$f(x) = \sum_{k=0}^{\infty} \frac{(x-x_i)^k}{k!} f^{(k)}(x_i) = \sum_{k=0}^{\infty} \frac{(x-x_i)^k}{k!} f_i^{(k)} \quad , \tag{27}$$

where, $f^{(k)}(x) = f(x)$ if $k = 0$ and $\frac{d^k f}{dx^k}$ otherwise. Application of (27) to nearest and next nearest neighbors to grid point i and truncation to the 4th order yields a set of four equations, namely

$$\begin{bmatrix} -2a & \frac{(-2a)^2}{2!} & \frac{(-2a)^3}{3!} & \frac{(-2a)^4}{4!} \\ -a & \frac{(-a)^2}{2!} & \frac{(-a)^3}{3!} & \frac{(-a)^4}{4!} \\ +a & \frac{(+a)^2}{2!} & \frac{(+a)^3}{3!} & \frac{(+a)^4}{4!} \\ +2a & \frac{(+2a)^2}{2!} & \frac{(+2a)^3}{3!} & \frac{(+2a)^4}{4!} \end{bmatrix} \begin{bmatrix} f_i^{(1)} \\ f_i^{(2)} \\ f_i^{(3)} \\ f_i^{(4)} \end{bmatrix} = \begin{bmatrix} f_{i-2} - f_i \\ f_{i-1} - f_i \\ f_{i+1} - f_i \\ f_{i+2} - f_i \end{bmatrix} \qquad (28)$$

The set of linear equations (28) provide numerical estimates for the first, second, third, and fourth derivatives of f at grid point i. In particular, the general form of the first and second derivative based on second nearest neighbors expansion reads

$$\begin{aligned} f_i^{(1)} &= \frac{f_{i-2} - 8f_{i-1} + 8f_{i+1} - f_{i+2}}{12a} \quad, \\ f_i^{(2)} &= \frac{-f_{i-2} + 16f_{i-1} - 30f_i + 16f_{i+1} - f_{i+2}}{12a^2} \quad, \end{aligned} \qquad (29)$$

respectively.

2.3 Boundary conditions implementation: "free" boundary conditions

Expressions above cease to be valid when the grid point becomes closest or next-to-closest to the boundary of the magnetic volume. Specific, accuracy preserving, expansions need to be worked out. The general principle in the present approach is to replace equations that are missing because of the lack of grid point(s) outside the magnetic volume by equations including explicit reference to boundary conditions, Eq. (17).

Consider first a point second to closest to boundary (see Fig. 3-b). Grid point $i + 2$ is missing for this particular geometry. However, defining x_R as the right boundary coordinate along the x axis, the last equation in (28) may, assuming $f^{(1)}(x_R)$ to be known along the boundary, be replaced by:

$$f^{(1)}(x_R) = f_i^{(1)} + (x_R - x_i)f_i^{(2)} + \frac{1}{2!}(x_R - x_i)^2 f_i^{(3)} + \frac{1}{3!}(x_R - x_i)^3 f_i^{(4)} \quad, \ (30)$$

a result stemming directly from the derivation of Taylor's expansion (27), namely

$$f^{(1)}(x) = \sum_{k=1}^{\infty} \frac{(x - x_i)^{k-1}}{(k - 1)!} f^{(k)}(x_i) \quad. \qquad (31)$$

For the geometry depicted in Fig. 3-b, $x_R - x_i = 3a/2$ and (28) becomes :

$$\begin{bmatrix} -2a & \frac{(-2a)^2}{2!} & \frac{(-2a)^3}{3!} & \frac{(-2a)^4}{4!} \\ -a & \frac{(-a)^2}{2!} & \frac{(-a)^3}{3!} & \frac{(-a)^4}{4!} \\ +a & \frac{(+a)^2}{2!} & \frac{(+a)^3}{3!} & \frac{(+a)^4}{4!} \\ 1 & \left(\frac{+3a}{2}\right) & \frac{(+3a/2)^2}{2!} & \frac{(+3a/2)^3}{3!} \end{bmatrix} \begin{bmatrix} f_{\mathrm{i}}^{(1)} \\ f_{\mathrm{i}}^{(2)} \\ f_{\mathrm{i}}^{(3)} \\ f_{\mathrm{i}}^{(4)} \end{bmatrix} = \begin{bmatrix} f_{\mathrm{i}-2} - f_{\mathrm{i}} \\ f_{\mathrm{i}-1} - f_{\mathrm{i}} \\ f_{\mathrm{i}+1} - f_{\mathrm{i}} \\ f^{(1)}(x_{\mathrm{R}}) \end{bmatrix} \qquad (32)$$

Similarly, for a point closest to boundary (see Fig. 3-c), grid points $i+1$ and $i+2$ are missing. The two first equations of (28) need now to be replaced by a single equation, whilst the two remaining equations need to be truncated to the third order. For the geometry illustrated in Fig. 3-c, the minimal set of equations now reads

$$\begin{bmatrix} -2a & \frac{(-2a)^2}{2!} & \frac{(-2a)^3}{3!} \\ -a & \frac{(-a)^2}{2!} & \frac{(-a)^3}{3!} \\ 1 & \left(\frac{+a}{2}\right) & \frac{(+a/2)^2}{2!} \end{bmatrix} \begin{bmatrix} f_{\mathrm{i}}^{(1)} \\ f_{\mathrm{i}}^{(2)} \\ f_{\mathrm{i}}^{(3)} \end{bmatrix} = \begin{bmatrix} f_{\mathrm{i}-2} - f_{\mathrm{i}} \\ f_{\mathrm{i}-1} - f_{\mathrm{i}} \\ f^{(1)}(x_{\mathrm{R}}) \end{bmatrix} \quad , \qquad (33)$$

where, $x_{\mathrm{R}} - x_{\mathrm{i}} = a/2$. In both cases, first and second derivatives are fully determined provided $f^{(1)}(x_{\mathrm{R}})$ be known along the boundary. The implementation of BC's is, however, not unique. For instance, Eq. 33 could include four internal mesh points instead of only three. *Donahue* and *Porter* [32] have evaluated the accuracy of several numerical schemes allowing for the evaluation of the exchange energy (4) and the enclosed derivatives. Their general conclusion is that the so-called "12-neighbors" scheme, i.e. 4 neighbors along each axis of the Euclidian space, is accuracy preserving up to order 4, at least for "free" BC's. The derivation above belongs to the "12-neighbors" class.

Eqs. 32 or 33 may be applied *mutatis mutandis* to the left boundary $x = x_{\mathrm{L}}$. Altogether, Eq. 28 and Eqs. akin to 32 and 33 fully specify the 1st, 2nd and 3rd derivatives of function $f(x)$ within the interval $]x_{\mathrm{L}}, x_{\mathrm{R}}[$, provided boundary values of the first derivatives *vs* x be known. For "free" BC's, $f^{(1)}(x_{\mathrm{L}}) = f^{(1)}(x_{\mathrm{R}}) \equiv 0$, or more generally, $\frac{\partial m_{x_{\mathrm{S}}}}{\partial x} = \frac{\partial m_{y_{\mathrm{S}}}}{\partial x} = \frac{\partial m_{z_{\mathrm{S}}}}{\partial x} = 0$ for a flat boundary perpendicular to x located at position x_{S}. Generalization to three dimensions in the Euclidian space proves straightforward. Even for "free" BC's, however, an evaluation of the relevant magnetization components along boundaries is still required in order to compute the contribution of surface charges to the demagnetizing field. Referring to Fig. 3-c, Taylor expansion (Eq. (27)) up to e.g. the third order yields

$$f(x_{\mathrm{R}}) = f_{\mathrm{i}} + (x_{\mathrm{R}} - x_{\mathrm{i}}) f_{\mathrm{i}}^{(1)} + \frac{1}{2!}(x_{\mathrm{R}} - x_{\mathrm{i}})^2 f_{\mathrm{i}}^{(2)} + \frac{1}{3!}(x_{\mathrm{R}} - x_{\mathrm{i}})^3 f_{\mathrm{i}}^{(3)} \quad , \quad (34)$$

where i here is the index of the mesh point closest to boundary. Assuming a constant charge density for the surface element centered on x_{R}, the surface charge $+\mu_0 M_{\mathrm{s}} (\mathbf{m} \cdot \mathbf{n})$ is simply $+\mu_0 M_{\mathrm{s}} m_{x_{\mathrm{R}}}$ with $m_{\mathrm{x}}(x) = f(x)$ in Eq. 34. Here also, generalization to three dimensions in the Euclidian space is straightforward.

Summarizing at this point, knowing the distribution $\mathbf{m(r)}$ inside a magnetic volume bounded by flat boundaries, all necessary derivatives of the magnetization components as well as estimates of surface charges are available through Taylor expansion and explicit use of BC's reading $\frac{\partial \mathbf{m}}{\partial \mathbf{n}} = 0$ in the case of "free" BC's. High accuracy (up to $O(h^4)$) may be preserved in this process.

As an example, the magnetization distribution within a soft and thin rectangular platelet is displayed in Fig. 4. The initial state was uniformly magnetized along the diagonal of the rectangle. At remanence, the magnetization becomes essentially uniform and parallel to the element's long edges, thus avoiding both volume and surface charges along the most part of the latter. Close to the extremities, however, the magnetization distribution is bending in such a way as to allow for a decrease of surface charges along the element short edges at the expense of exchange and volume magnetostatic energy. Actually, in sub-micron size thin soft magnetic elements, the number of possible magnetization states becomes discrete [33, 34, 35, 36, 37]. The magnetization state shown in Fig. 4 is called a S-State. Platelets displaying S-States may be found in four variants according to the direction of the magnetization in the main section of the element ($\approx +x$ or $\approx -x$), and the magnetization component along the element short edges ($+y$ or $-y$). Reversing the magnetization rotation direction close to one extremity would lead to a so-called C-State with, again, four possible variants characterized by a single energy.
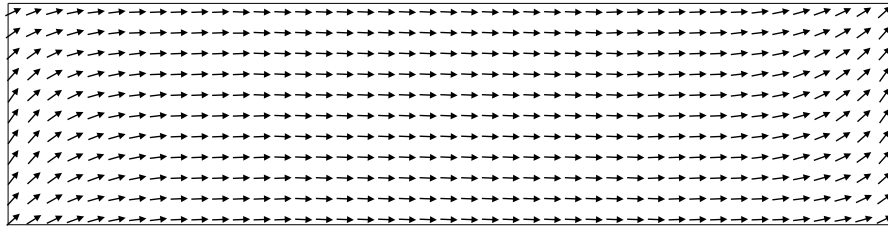

Fig. 4. Magnetization distribution characteristic of a so-called S-State in a thin film element: the magnetization keeps parallel to the long edges of the element, thus avoiding both volume and surface charges along the most part of the latter. Close to the extremities, however, a gradual bending of the magnetization distribution allows for a decrease of surface charges along the element short edges at the expense of exchange and volume magnetostatic energy. $Ni_{80}Fe_{20}$ like materials parameters (Exchange constant: $A = 1.3 \times 10^{-11}$ J/m, saturation magnetization $M_s = 800$ kA/m); Dimensions: 500 nm $\times$ 125 nm $\times$ 3 nm; Meshing: $256 \times 64 \times 1$ (One-layer-of-cells type simulation).

Although the thickness in that particular element remains smaller than the exchange length for the material considered (3 nm *vs* 5.68 nm), the decomposition of the element into three layers of cells reveals interesting features of the magnetization distribution at equilibrium. The minute splay across the thickness of the magnetization displayed in Fig. 5 actually leads to a decrease

of both the exchange and the magnetostatic energies (see the caption of Fig. 5 for details). Fig. 5 emphasizes the stringent need for rather small mesh sizes (a relatively small fraction of the exchange length) if the fine features of the magnetization distribution are to be revealed with a satisfying accuracy.
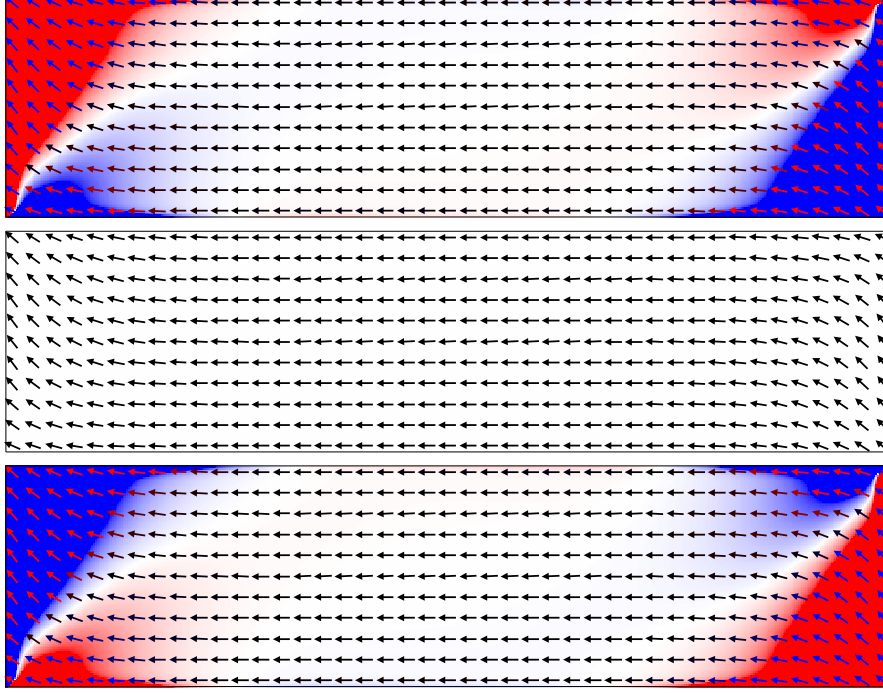

Fig. 5. Magnetization distribution characteristic of a so-called S-State in a thin film element owing to 3-Dimensional micromagnetics. Close to the upper left boundary, the in-plane magnetization is fanning-in, leading to positive volume charges; in the top and bottom computation cell-layers (top and bottom figures, respectively), the z-component (out-of-plane) of the magnetization is positive (red background) and negative (blue background), respectively. The fanning-out of the magnetization along the normal to the magnetic element allows for charge compensation between the in-plane and out-of-plane magnetization distributions, leading to an overall reduction of both the exchange and demagnetizing field energy. The magnetization distribution around the bottom right corner behaves symmetrically (in-plane fanning-out, out-of-plane fanning-in). $Ni_{80}Fe_{20}$ like materials parameters (Exchange constant: $A = 1.3 \times 10^{-11}$ J/m, saturation magnetization $M_s = 800$ kA/m) ; Dimensions: 500 nm $\times$ 125 nm $\times$ 3 nm; Meshing: $511 \times 127 \times 3$.

2.4 Boundary conditions implementation: extended boundary conditions

Additional work needs to be performed when dealing with general boundary conditions (17). General boundary conditions are expressed in terms of boundary values for the magnetization. Boundary magnetization values (look at Eq.(34)) are functions of derivatives defined at given mesh points that themselves depend on specific derivatives along boundaries (see Eqs.(32) and (33)). It ensues that for each boundary point where an estimate of a boundary derivative is required, an implicit equation needs to be solved. Consider again the boundary point in Fig. 3-b or c. The requested boundary derivatives read $\frac{\partial m_x(x_R)}{\partial x}, \frac{\partial m_y(x_R)}{\partial x}, \frac{\partial m_z(x_R)}{\partial x}$. In components form, neglecting the J_2 biquadratic exchange term, extended boundary conditions for the right boundary (normal along $+x$) read:

$$
\begin{aligned}
\frac{\partial m_x^R}{\partial x} &= \frac{K_S}{A} m_x^R \left[1 - m_x^{R2} \right] - \frac{J_1}{2A} \left[\left(\mathbf{m}^R \cdot \mathbf{m}' \right) m_x^R - m_x' \right] \\
\frac{\partial m_y^R}{\partial x} &= -\frac{K_S}{A} m_x^{R2} m_y^R - \frac{J_1}{2A} \left[\left(\mathbf{m}^R \cdot \mathbf{m}' \right) m_y^R - m_y' \right] \quad (35) \\
\frac{\partial m_z^R}{\partial x} &= -\frac{K_S}{A} m_x^{R2} m_z^R - \frac{J_1}{2A} \left[\left(\mathbf{m}^R \cdot \mathbf{m}' \right) m_z^R - m_z' \right] \quad ,
\end{aligned}
$$

where $\mathbf{m}^R = \mathbf{m}(x_R)$. Combined with relations akin (34) and (32) or (33), Eq. (35) provides a set of non-linear equations (3rd order in the general case) in the variables m_x^R, m_y^R, m_z^R that may easily be solved *via* e.g. Newton's method. A proper numerical implementation ensures that extended BC's are strictly equivalent to "free" BC's if $K_S = J_1 = 0$.

2.5 Energy

The energy to be evaluated embodies the exchange, anisotropy, Zeeman and demagnetizing field energies that sum-up to the total energy expressed in (3). Additional energy terms do arise from extended boundary conditions, namely $E_{K_S} = \int_S \varepsilon_{K_S} \, dS$ and $E_J = \int_S \varepsilon_J \, dS$. Owing to the numerical scheme outlined above, both the magnetization and the effective field are meant to be continuous functions of position sampled at regularly spaced volume mesh points. The magnetization also needs to be evaluated at the center of surface tiles in order to satisfy to BC's and allow for the computation of surface charge densities. Whenever the magnetization is evaluated, its unit norm ($\mathbf{m} \cdot \mathbf{m} = 1$) must be enforced.

Zeeman, anisotropy and exchange energy

Consider the right-hand expression of the exchange energy in (4). Its discrete counterpart reads :

$$E_{\text{exch}} = -A\,V_{\text{Cell}} \sum_{i,j,k} \left[\langle \mathbf{m} \rangle \cdot \left(\langle \frac{\partial^2 \mathbf{m}}{\partial x^2} \rangle + \langle \frac{\partial^2 \mathbf{m}}{\partial y^2} \rangle + \langle \frac{\partial^2 \mathbf{m}}{\partial z^2} \rangle \right) \right] \quad , \qquad (36)$$

where, $\langle \mathbf{V} \rangle$ is the average value of $\mathbf{V}$ within a given cell. As discussed in section 3, however, the cell-averaged value of any variable is equal to its value at cell center, be it a volume cell or a surface tile, to order 2, because all nearest order corrective terms sum up to zero. Although higher order corrections may be worked out, such corrective actions have almost no incidence on the numerical estimate of the relevant energy, as exemplified in Fig. 6-a. The same conclusion holds true for the estimate of the Zeeman (applied field) and anisotropy energies as demonstrated in sections 3.1 and 3.2, respectively. Similar arguments also apply to energy terms linked to specific boundary conditions for which the energy densities in the continuum limit are given by (14) and (15).

Demagnetizing field (or magnetostatic) energy

In the present field-based scheme, quantities that are constant per cell or tile are the magnetization divergence and the surface charge density. It is therefore natural to seek an expression for the energy that embodies these quantities. An expression for the energy is readily available if assuming the scalar potential (20) to be known (up to this point, only the field has been evaluated at discrete points). If either the magnetization divergence or the surface charge density are piecewise constant, the scalar potential is not. Therefore, the transcription of the continuous energy expression

$$E_{\text{demag}} = \frac{1}{2} \int_V \lambda_{\text{V}}(\mathbf{r}) \Phi_{\text{d}}(\mathbf{r})\, d^3\mathbf{r} + \frac{1}{2} \int_S \sigma_{\text{S}}(\mathbf{r}) \Phi_{\text{d}}(\mathbf{r})\, d^2\mathbf{r} \quad , \qquad (37)$$

into a discrete summation requests the evaluation of the average value of the potential $< \Phi_{\text{d}} >$ over each cell or tile (see Section 3.4 where a similar procedure is applied to the evaluation of the average field within a cell). Eq. (37) thus becomes:

$$E_{\text{demag}} = \frac{1}{2} \sum_{i,j,k} \left[\lambda_{\text{V}}(i,j,k) \langle \Phi_{\text{d}}(i,j,k) \rangle \right] + \frac{1}{2} \sum_{l,m,n} \left[\sigma_{\text{S}}(l,m,n) \langle \Phi_{\text{d}}(l,m,n) \rangle \right] \quad ,$$
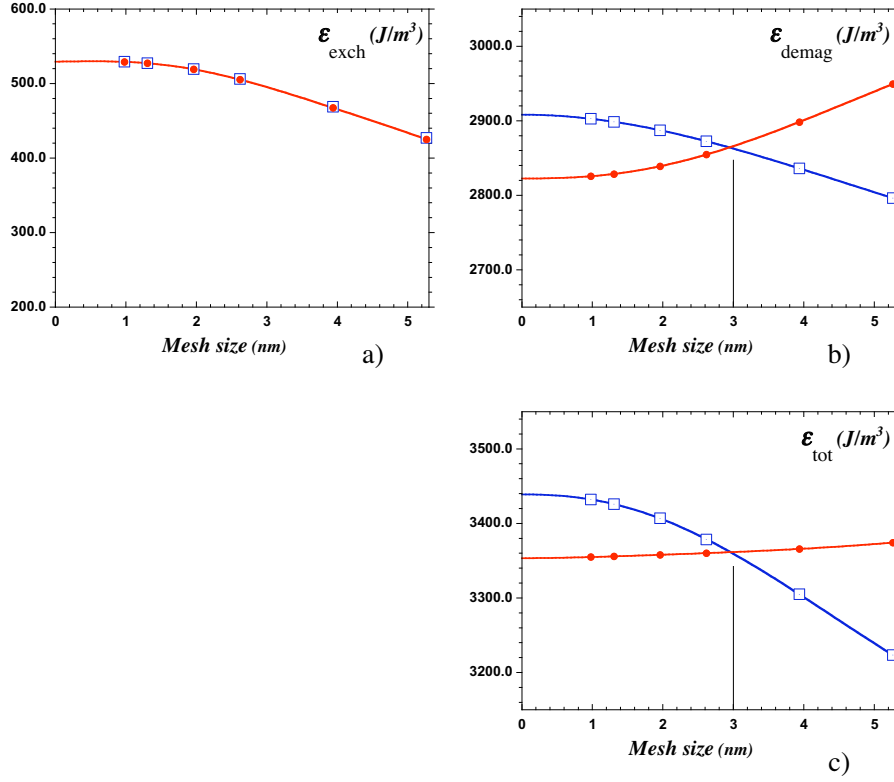$$\qquad (38)$$

where,

Fig. 6. Energy per unit volume *vs* in-plane mesh size for the S-State magnetization distribution shown in Fig. 4. a) Exchange, b) magnetostatic, c) total energy per unit volume. Open and full symbols refer to direct and cell-averaged summation, respectively. The magnetostatic energy is approximated by Eqs.(41) and (38) for direct and cell-averaged summation, respectively. The fitting curves should be viewed as mere guides to the eye. $Ni_{80}Fe_{20}$ like materials parameters (Exchange constant: $A = 1.3 \times 10^{-11}$ J/m, saturation magnetization $M_s = 800$ kA/m) ; Dimensions: 500 nm $\times$ 125 nm $\times$ 3 nm; One-layer-of-cells type simulation.

$$4\pi\mu_0\, V_{\mathrm{Cell}}\, \langle \Phi_{\mathrm{d}}(i,j,k) \rangle =$$

$$\sum_{i',j',k'} \lambda_{\mathrm{V}}(i',j',k') \int_{V(i,j,k)} d^3\mathbf{r} \int_{V(i',j',k')} \frac{1}{|\mathbf{r}-\mathbf{r}'|}\, d^3\mathbf{r}' +$$

$$\sum_{l',m',n'} \sigma_{\mathrm{S}}(l',m',n') \int_{V(i,j,k)} d^3\mathbf{r} \int_{S(l',m',n')} \frac{1}{|\mathbf{r}-\mathbf{r}'|}\, d^2\mathbf{r}' \tag{39}$$

for volume cells, and

$$4\pi\mu_0 \, S_{\text{Tile}} \, \langle \Phi_{\text{d}}(l,m,n) \rangle =$$

$$\sum_{i',j',k'} \lambda_{\text{V}}(i',j',k') \int_{S(l,m,n)} d^2\mathbf{r} \int_{V(i',j',k')} \frac{1}{|\mathbf{r}-\mathbf{r'}|} \, d^3\mathbf{r'} +$$

$$\sum_{l',m',n'} \sigma_{\text{S}}(l',m',n') \int_{S(l,m,n)} d^2\mathbf{r} \int_{S(l',m',n')} \frac{1}{|\mathbf{r}-\mathbf{r'}|} \, d^2\mathbf{r'} \tag{40}$$

for surface tiles. Cell or tile average scalar potential evaluation requires integrals of type F^{222}, F^{221} plus circular permutations, F^{220} plus circular permutations, where $F^{000} = \frac{1}{r}$, $F^{100} = \int F^{000} dx$, $F^{110} = \int F^{000} dx dy$ etc [6]. All necessary integrals are tabulated in Appendix B. For instance, the contribution of a tile belonging to the ($xy \equiv [110]$) surface to the averaged potential within a volume cell ($\equiv [111]$) involves the F^{221} integral etc. All interaction integrals are positive definite so that interactions between charges of similar sign, whether volume or surface, contribute positively to the energy whereas interactions between opposite sign charges contribute negatively.

Although potential theory is the only approach to energy evaluation consistent with the present field-based model, a rough estimate of the magnetostatic energy may still be gained from the numerical equivalent to Eq. (3), namely

$$E_{\text{demag}} = -\frac{1}{2}\mu_0 V_{\text{Cell}} \sum_{i,j,k} \left(\mathbf{H}_{\text{d}}(i,j,k) \right) \cdot \mathbf{M}(i,j,k) \quad , \tag{41}$$

where it is implicitly assumed that the magnetization and the demagnetizing field are constant within each volume cell.

Results pertaining to the S-State in Fig. 4 are displayed in Fig. 6. The exchange energy per unit volume *vs* mesh size (Fig. 6-a) is seen to depend very little on the use or not of cell-averaged variables in (36). Convergence of the exchange energy on the other hand is only attained for rather small mesh sizes. Markedly different behaviors for the demagnetizing field energy are obtained when using cell-averaged potential theory (Eq.(38)) or the rough estimate (41) (Fig. 6-b). In both cases, small mesh sizes are required in order to define the asymptotic value of the magnetostatic energy, thus following a trend similar to that of the exchange energy. More surprising at first sight is the fact that both estimates of the magnetostatic energy do not converge to the same value for a vanishing mesh size. It ought to be noted that the best agreement between the two kinds of estimates is obtained for cubic cells (size 3 nm, here). It may therefore be concluded that the rough estimate (41) becomes particularly poor for cells aspect ratios markedly departing from unity. The total energy per unit volume *vs* mesh size consistent with the assumptions of the present numerical model is shown as full symbols in Fig. 6-c. It appears relatively independent of mesh size although this result is physically meaningless: only the respective asymptotic values [38] of the energy contributions are representative of the physical reality. The exchange and magnetostatic energies actually display opposite curvature convergence behaviors, pointing at a

subtle change in the balance between exchange and magnetostatic interactions with decreasing mesh size.

3 Finite difference micromagnetics: energy-based approach

In an energy-based approach, the magnetic energy is given primacy, and is computed directly from the discretized magnetization, whereas the effective field is derived from the resultant energy. The effective field obtained in this manner is a cell-averaged field. This method is obviously convenient if one is interested in finding equilibrium magnetization patterns via direct energy minimization (using, for example, conjugate-gradient methods), but also has the advantage that the energy, being an integral quantity, has less variation than the field and is therefore more easily approximated. As noted in Sec. 2.1, the demagnetizing field can diverge at corners of a sample, yet this logarithmic divergence is integrable, so that the energy contained in any discretization cell remains finite. This effect is seen too in Fig. 6-b, where the result using (41) leads to an incorrect result, even in the small cell limit. Although the discretization in this example is sufficient to represent variations in the magnetization, it does not pick up variations in the demagnetizing field along the film normal [16, 39]. To correct for this one has to either move to a multi-layer simulation, or else use a potential averaging approach as in (38) or as discussed in this section.

3.1 Zeeman energy

As stated before, Zeeman energy is the magnetostatic energy from the interaction of a given magnetization state with an external field,

$$E_{\mathrm{Z}} = -\mu_0 \int_V \mathbf{M} \cdot \mathbf{H}_{\mathrm{app}} \, d^3 r. \tag{42}$$

Here $\mathbf{H}_{\mathrm{app}}$ includes fields directly applied, and also fields resulting from currents inside the device, i.e.,

$$\mathbf{H}_{\mathrm{current}} = \frac{1}{4\pi} \int_V \mathbf{J}(\mathbf{r}') \times \frac{\mathbf{r} - \mathbf{r}'}{|\mathbf{r} - \mathbf{r}'|^3} \, d^3 r'. \tag{43}$$

Assuming that both $\mathbf{M}$ and $\mathbf{H}_{\mathrm{app}}$ are twice differentiable, we can write

$$\mathbf{M}(\mathbf{r}) = \mathbf{M}(\mathbf{r}_i) + B\left(\mathbf{r} - \mathbf{r}_i\right) + O(\|\mathbf{r} - \mathbf{r}_i\|^2) \tag{44}$$

$$\mathbf{H}_{\mathrm{app}}(\mathbf{r}) = \mathbf{H}_{\mathrm{app}}(\mathbf{r}_i) + C\left(\mathbf{r} - \mathbf{r}_i\right) + O(\|\mathbf{r} - \mathbf{r}_i\|^2) \tag{45}$$

where B and C are the 3×3 matrices corresponding to the partial derivatives of $\mathbf{M}$ and $\mathbf{H}_{\mathrm{app}}$, respectively, and $\mathbf{r}_i$ is an arbitrary point suitably close to $\mathbf{r}$. Consider this simple approximation to the Zeeman energy:

$$E_{\mathrm{Z}} \approx -\mu_0 \sum_i \mathbf{M}(\mathbf{r}_i) \cdot \mathbf{H}_{\mathrm{app}}(\mathbf{r}_i)|V_i|, \tag{46}$$

where the index i runs over all cells in the simulation, $\mathbf{r}_i$ denotes the center of the rectangular cell i, and $|V_i|$ is the volume of cell i. Given (44) and (45), we estimate the error in (46) as

$$\left| E_{\mathrm{Z}} - (-\mu_0) \sum_i \mathbf{M}(\mathbf{r}_i) \cdot \mathbf{H}_{\mathrm{app}}(\mathbf{r}_i)|V_i| \right|$$

$$\leq \mu_0 \sum_i \left| \int_{V_i} \mathbf{M}(\mathbf{r}) \cdot \mathbf{H}_{\mathrm{app}}(\mathbf{r}) - \mathbf{M}(\mathbf{r}_i) \cdot \mathbf{H}_{\mathrm{app}}(\mathbf{r}_i)\, d^3 r \right| \tag{47}$$

$$\leq \mu_0 \sum_i \left| \int_{V_i} \mathbf{M}(\mathbf{r}_i)^T C\,(\mathbf{r} - \mathbf{r}_i) + \mathbf{H}_{\mathrm{app}}(\mathbf{r}_i)^T B\,(\mathbf{r} - \mathbf{r}_i) \right.$$

$$\left. + O(\|\mathbf{r} - \mathbf{r}_i\|^2)\, d^3 r \right|, \tag{48}$$

where $\cdot^T$ denotes the vector transpose. Since $\mathbf{r}_i$ is at the center of the rectangular cell V_i,

$$\int_{V_i} (\mathbf{M}(\mathbf{r}_i)^T C + \mathbf{H}_{\mathrm{app}}(\mathbf{r}_i)^T B)(\mathbf{r} - \mathbf{r}_i)\, d^3 r = 0 \tag{49}$$

because the integrand is an odd function with respect to $\mathbf{r}_i$. Thus we see that

$$\left| E_{\mathrm{Z}} - (-\mu_0) \sum_i \mathbf{M}(\mathbf{r}_i) \cdot \mathbf{H}_{\mathrm{app}}(\mathbf{r}_i)|V_i| \right| \leq \mu_0 \sum_i \int_{V_i} O(\|\mathbf{r} - \mathbf{r}_i\|^2)\, d^3 r \tag{50}$$

$$\leq O(\Delta^2)|V|, \tag{51}$$

where $|V| = \sum_i |V_i|$ is the total volume of the space, and Δ is the maximum cell dimension.

In this approximation, all of the $\mathbf{M}(\mathbf{r}_i) \cdot \mathbf{H}_{\mathrm{app}}(\mathbf{r}_i)$ terms are weighted equally. Higher order methods can be obtained by varying the weights, similar to the well-known Simpson's rule [40, 41].

The discretized field expression derived from this approximation to the energy is simply

$$\mathbf{H}_{\mathrm{Z},i} = \mathbf{H}_{\mathrm{app}}(\mathbf{r}_i). \tag{52}$$

3.2 Magnetocrystalline anisotropy energy

Magnetocrystalline anisotropy energy models the preferential magnetization orientation in a material, and depends chiefly on the crystalline structure of the material. For uniaxial materials the energy is given by

$$E_{\mathrm{K,uniaxial}} = -\int_V K_1 (\mathbf{m} \cdot \mathbf{u})^2\, d^3 r, \tag{53}$$

where K_1 is the material anisotropy coefficient (in J/m^3), $\mathbf{m}$ is the unit magnetization direction ($\mathbf{M}/M_\mathrm{s}$), and $\mathbf{u}$ is the (unit) anisotropy axis. If K_1 is positive, then $\mathbf{u}$ is the easy axis, while if K_1 is negative then $\mathbf{u}$ is normal to the easy plane. For some materials, a second term $K_2 \sin^4 \phi$ is important, where K_2 is a second anisotropy coefficient and ϕ is the angle between $\mathbf{m}$ and $\mathbf{u}$. This equation should be modified at material interfaces and defects [42].

For cubic materials with crystal axes oriented parallel to the coordinate axes, the energy takes the form

$$E_{\mathrm{K,cubic}} = \int_V K_1(m_x^2 m_y^2 + m_y^2 m_z^2 + m_z^2 m_x^2) + K_2(m_x^2 m_y^2 m_z^2)\, d^3r. \qquad (54)$$

For a rotated crystal orientation, m_x should be replaced with the projection of $\mathbf{m}$ onto the first coordinate axis, m_y with the projection onto the second (orthogonal) axis, and m_z with the projection onto the remaining axis.

If we assume that $\mathbf{m}$, $\mathbf{u}$, K_1 and K_2 are twice differentiable, at least within each cell, then we can expand the integrands in (53) and (54) in a the manner of (44) and (45), and obtain an analogous discrete approximation for the magnetocrystalline anisotropy energy. In the uniaxial case this is

$$E_{\mathrm{K,uniaxial}} \approx -\sum_i K_1(\mathbf{r}_i)\, (\mathbf{m}(\mathbf{r}_i) \cdot \mathbf{u}(\mathbf{r}_i))^2\, |V_i|, \qquad (55)$$

and for the cubic we have

$$E_{\mathrm{K,cubic}} \approx \sum_i \big[K_1(\mathbf{r}_i)\, \big(\mathbf{m}_x^2(\mathbf{r}_i)\mathbf{m}_y^2(\mathbf{r}_i) + \mathbf{m}_y^2(\mathbf{r}_i)\mathbf{m}_z^2(\mathbf{r}_i) + \mathbf{m}_x^2(\mathbf{r}_i)\mathbf{m}_z^2(\mathbf{r}_i)\big)$$
$$+ K_2(\mathbf{r}_i)\, \big(\mathbf{m}_x^2(\mathbf{r}_i)\mathbf{m}_y^2(\mathbf{r}_i)\mathbf{m}_z^2(\mathbf{r}_i)\big) \big]\, |V_i|. \qquad (56)$$

Using the same argument as in the Zeeman energy section, these approximations are also seen to be of order Δ^2.

The discretized field expressions derived from the discretized energies are

$$H_{\mathrm{K,uniaxial},i} = 2K_1(\mathbf{r}_i)\, (\mathbf{m}(\mathbf{r}_i) \cdot \mathbf{u}(\mathbf{r}_i))\, \mathbf{u}(\mathbf{r}_i)/\mu_0 M_\mathrm{s} \qquad (57)$$
$$H_{\mathrm{K,cubic},i} = -2\, D(\mathbf{r}_i)\mathbf{m}(\mathbf{r}_i)/\mu_0 M_\mathrm{s}, \qquad (58)$$

where D is the diagonal matrix with entries

$$D_{11} = K_1(\mathbf{r}_i)\, \big(m_y^2(\mathbf{r}_i) + m_z^2(\mathbf{r}_i)\big) + K_2(\mathbf{r}_i)m_y^2(\mathbf{r}_i)m_z^2(\mathbf{r}_i) \qquad (59)$$
$$D_{22} = K_1(\mathbf{r}_i)\, \big(m_x^2(\mathbf{r}_i) + m_z^2(\mathbf{r}_i)\big) + K_2(\mathbf{r}_i)m_x^2(\mathbf{r}_i)m_z^2(\mathbf{r}_i) \qquad (60)$$
$$D_{33} = K_1(\mathbf{r}_i)\, \big(m_x^2(\mathbf{r}_i) + m_y^2(\mathbf{r}_i)\big) + K_2(\mathbf{r}_i)m_x^2(\mathbf{r}_i)m_y^2(\mathbf{r}_i). \qquad (61)$$

3.3 Exchange energy

As noted in Sec. 1, the exchange energy may be represented using either of the expressions in (4). In practice, the latter relation,

$$E_{\mathrm{exch}} = -\int_V A\, \mathbf{m} \cdot \left(\frac{\partial^2 \mathbf{m}}{\partial x^2} + \frac{\partial^2 \mathbf{m}}{\partial y^2} + \frac{\partial^2 \mathbf{m}}{\partial z^2} \right) d^3r. \qquad (62)$$

is somewhat easier to work with and is the form used in the following discussion.

The first step in providing a numerical approximation to (62) is to find a discrete form for the second derivative operator. As mentioned in section 2.2, the simplest approximation, which holds if $\mathbf{m}$ is four times differentiable, is

$$\frac{\partial^2 \mathbf{m}}{\partial x^2}(\mathbf{r}) = \frac{1}{\Delta_x^2} \left(\mathbf{m}(\mathbf{r} + \Delta_x \hat{x}) - 2\mathbf{m}(\mathbf{r}) + \mathbf{m}(\mathbf{r} - \Delta_x \hat{x}) \right) + O(h^2), \qquad (63)$$

where Δ_x is the discretized cell dimension along the $\hat{x}$ direction. The analogous equations for $\partial^2 \mathbf{m}/\partial y^2$ and $\partial^2 \mathbf{m}/\partial z^2$ (involving Δ_y and Δ_z), lead to a seven point approximation to the integrand in (62), involving $\mathbf{m}$ at the point $\mathbf{r}_i$ and its six closest neighbors:

$$E_{\text{exch}} \approx -\sum_i |V_i| A \sum_j \mathbf{m}(\mathbf{r}_i) \cdot \left(\mathbf{m}(\mathbf{r}_i + \epsilon_j) - \mathbf{m}(\mathbf{r}_i) \right) / |\epsilon_j|^2. \qquad (64)$$

Here $\mathbf{r}_i + \epsilon_j$, varying over j, specifies each of the six nearest neighbors to $\mathbf{r}_i$ in the discretized mesh. By the same argument used in the previous two sections, this estimate will be of $O(\Delta^2)$. The corresponding expression for the discretized exchange field is

$$H_{\text{exch}} = \frac{2A}{\mu_0 M_{\text{s}}} \sum_j \left(\mathbf{m}(\mathbf{r}_i + \epsilon_j) - \mathbf{m}(\mathbf{r}_i) \right) / |\epsilon_j|^2. \qquad (65)$$

One may be tempted to replace $\mathbf{m}(\mathbf{r}_i) \cdot \mathbf{m}(\mathbf{r}_i)$ in (64) with $|\mathbf{m}|^2 = 1$, obtaining

$$E_{\text{exch}} \approx -\sum_i |V_i| A \sum_j \left(\mathbf{m}(\mathbf{r}_i) \cdot \mathbf{m}(\mathbf{r}_i + \epsilon_j) - 1 \right) / |\epsilon_j|^2, \qquad (66)$$

or to drop the "-1" altogether, which shifts E_{exch} by a constant amount without affecting the exchange field. Either way, however, leads to numerical problems because the term $\mathbf{m}(\mathbf{r}_i) \cdot \mathbf{m}(\mathbf{r}_i + \epsilon_j)$ effectively loses significant precision in the common case where $\mathbf{m}(\mathbf{r}_i)$ and $\mathbf{m}(\mathbf{r}_i + \epsilon_j)$ are nearly parallel. This can be seen by realizing that $\mathbf{m}(\mathbf{r}_i) \cdot \mathbf{m}(\mathbf{r}_i + \epsilon_j) = \cos\theta$, where θ is the angle between $\mathbf{m}(\mathbf{r}_i)$ and $\mathbf{m}(\mathbf{r}_i + \epsilon_j)$, and $\cos\theta \approx 1 - \theta^2/2$. The torque depends on the component perpendicular to $\mathbf{m}(\mathbf{r}_i)$, which is represented by the θ^2 term. If $|\theta| \ll 1$, then when stored with a finite number of digits the expression $1 - \theta^2/2$ loses a great deal of the precision in θ^2. On the other hand, if one first subtracts $\mathbf{m}(\mathbf{r}_i)$ from $\mathbf{m}(\mathbf{r}_i + \epsilon_j)$ as in (64) then the dot product will be between two nearly perpendicular vectors, and precision is significantly retained [39].

Large angles between neighboring spins $\mathbf{m}(\mathbf{r}_i)$ and $\mathbf{m}(\mathbf{r}_i + \epsilon_j)$ also cause problems, but of a rather different nature. Here the problem arises because (64) always underestimates the exchange energy, and the larger the neighboring spin angle θ the larger the underestimate. As a result, magnetization

configurations with regions of high exchange energy that are located between grid points tend to have overall smaller total exchange energy than otherwise identical configurations shifted so that the points of high exchange energy are on or near grid points. This can cause artificial, discretization-induced pinning of high exchange energy structures such as vortices [43] or induce a Peierl's like friction for Bloch points motion [44]. Figure 7 illustrates this problem on a small, thin plate. In this example, maximum pinning is 18 mT, which occurs with an in-plane cell size of just under 7 nm. Moreover, the pinning is found to be non-monotonic with Δ, at first worsening as Δ is decreased, only abating after the vortex core is resolved.
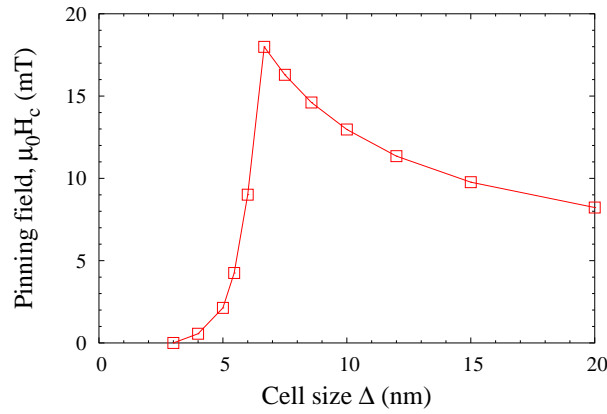
Fig. 7. Discretization induced vortex pinning fields for a 120 nm × 120 nm × 3 nm $Ni_{80}Fe_{20}$ (M_s=800 kA/m, A=13 pJ/m, K=0 J/m^3) plate, as a function of in-plane discretization cell size (one-layer-of-cells type simulations). Initial zero-field magnetization configuration is an equilibrium centered vortex state. Field is applied in-plane, parallel to plate edge, and gradually increased until vortex jumps from one discretization cell to the next.

A related issue can occur in under-meshed 180° Néel walls [45]. If the angle between neighboring spins across the center of the wall is too large, then the wall demagnetizing field can overwhelm the coarse mesh weakened exchange field and force the Néel wall to collapse into a structure where the entire wall is squeezed between adjacent spins, as illustrated in Fig. 8(a). The problem is fixed when a sufficiently fine mesh is used, as in Fig. 8(b).

Simulations in Figs. 7 and 8 were performed using the OOMMF public code [46].
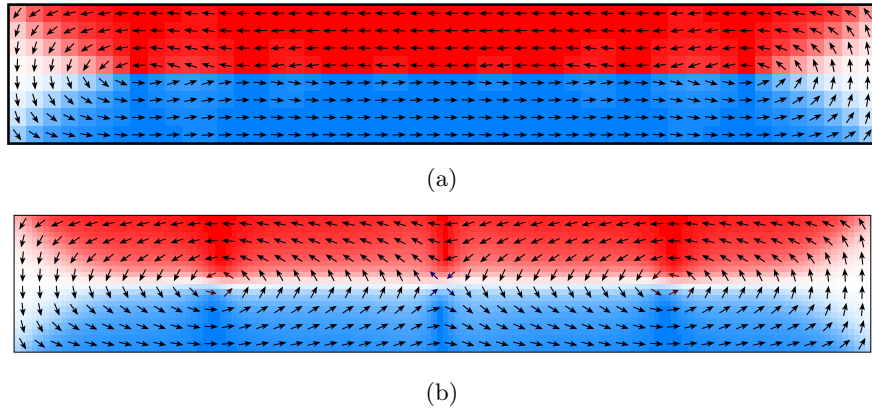
(a)

(b)

Fig. 8. Néel wall in 750 nm × 120 nm × 30 nm $Ni_{80}Fe_{20}$ rectangle, equilibrium states. (Same material parameters as quoted in Fig. 7.) (**a**) Wall collapses in coarse grid simulation (Δ=15 nm), as compared to (**b**) fully resolved wall using fine grid (Δ=5 nm). Color indicates x-axis component of the magnetization. Multi-layer cubic cells used in both simulations.

3.4 Self-magnetostatic energy

Self-magnetostatic, or demagnetization energy, is the energy associated with dipole-dipole magnetostatic interactions of material within itself. It is described by

$$E_{\text{demag}} = -\frac{\mu_0}{2} \int_V \mathbf{M} \cdot \mathbf{H}_{\text{d}} \, d^3r, \tag{67}$$

where the demagnetization field $\mathbf{H}_{\text{d}}$ at position r is

$$\mathbf{H}_{\text{d}}(\mathbf{r}) = -\frac{1}{4\pi} \int_V \nabla \cdot \mathbf{M}(\mathbf{r}') \frac{\mathbf{r} - \mathbf{r}'}{|\mathbf{r} - \mathbf{r}'|^3} \, d^3r' + \frac{1}{4\pi} \int_S \hat{\mathbf{n}}(\mathbf{r}') \cdot \mathbf{M}(\mathbf{r}') \frac{\mathbf{r} - \mathbf{r}'}{|\mathbf{r} - \mathbf{r}'|^3} \, d^2r'. \tag{68}$$

Eq.(68)) is identical to (21) and displayed here anew for convenience. Note that E_{demag} involves long range interactions, and in terms of $\mathbf{M}$ requires integration over $V \times V$.

If we let $\mathbf{g}(\mathbf{r}) = \mathbf{r}/|\mathbf{r}|^3$, then integration by parts allows one to rewrite (68) as

$$\mathbf{H}_{\text{d}}(r) = -\frac{1}{4\pi} \int_V \nabla \mathbf{g}(\mathbf{r} - \mathbf{r}') \mathbf{M}(\mathbf{r}') \, d^3r'. \tag{69}$$

From this formulation it is clear an approximation to $\mathbf{M}$ of the form (44) is sufficient to produce an approximation to $\mathbf{H}_{\text{d}}$ of second order, and moreover

that at this level of approximation the linear portion of $\mathbf{M}$ can be ignored. Thus we have

$$\mathbf{H}_{\mathrm{d}}(\mathbf{r}) = -\frac{1}{4\pi} \sum_i \int_{V_i} \nabla \mathbf{g}(\mathbf{r} - \mathbf{r}') \mathbf{M}(\mathbf{r}'_i) \, d^3 r' + O(\Delta^2) \tag{70}$$

$$= \frac{1}{4\pi} \sum_i \int_{S_i} \hat{\mathbf{n}}(\mathbf{r}') \cdot \mathbf{M}(\mathbf{r}'_i) \frac{\mathbf{r} - \mathbf{r}'}{|\mathbf{r} - \mathbf{r}'|^3} \, d^2 r' + O(\Delta^2). \tag{71}$$

This shows that, to second order, the demagnetization field at point $\mathbf{r}$ can be computed by treating each cell in the discretization as a uniformly magnetized block. Likewise, second order accuracy can be maintained in (67) by replacing $\mathbf{M}$ in each cell with its value at the center, so we have

$$E_{\mathrm{demag}} \approx -\frac{\mu_0}{8\pi} \sum_{i,j} \int_{V_i} \mathbf{M}(\mathbf{r}_i) \cdot \int_{S_j} \mathbf{M}(\mathbf{r}'_j) \cdot \hat{\mathbf{n}}(\mathbf{r}') \frac{\mathbf{r} - \mathbf{r}'}{|\mathbf{r} - \mathbf{r}'|^3} \, d^2 r' \, d^3 r \tag{72}$$

$$\approx -\frac{\mu_0}{8\pi} \sum_{i,j} \mathbf{M}^T(\mathbf{r}_i) \left(\int_{V_i} \int_{S_j} \frac{\mathbf{r} - \mathbf{r}'}{|\mathbf{r} - \mathbf{r}'|^3} \hat{\mathbf{n}}^T(\mathbf{r}') \, d^2 r' \, d^3 r \right) \mathbf{M}(\mathbf{r}_j). \tag{73}$$

This can be rewritten as

$$E_{\mathrm{demag}} \approx \frac{\mu_0}{2} \sum_{i,j} |V_i| \, \mathbf{M}^T(\mathbf{r}_i) N(\mathbf{r}_i, \mathbf{r}_j) \mathbf{M}(\mathbf{r}_j), \tag{74}$$

where $N(\mathbf{r}_i, \mathbf{r}_j)$ is the 3×3 matrix arising from the 5-fold integration in (73) divided by $-4\pi |V_i|$. The term $(\mu_0 |V_i|/2) \, \mathbf{M}^T(\mathbf{r}_i) N(\mathbf{r}_i, \mathbf{r}_j) \mathbf{M}(\mathbf{r}_j)$ is seen to be the (exact) magnetostatic energy arising between uniformly magnetized cells at positions $\mathbf{r}_i$ and $\mathbf{r}_j$. It is clear from the definition that N depends only on the difference $\mathbf{r}_i - \mathbf{r}_j$, so $N(\mathbf{r}_i, \mathbf{r}_j) = N(\mathbf{r}_i - \mathbf{r}_j) = N_{i-j}$.

If we compute the effective demagnetization field from (74), we obtain

$$\mathbf{H}_{\mathrm{d,i}} = -\sum_j N_{i-j} \mathbf{M}_j. \tag{75}$$

Note that as elsewhere in Sec. 3, $\mathbf{H}_{\mathrm{d,i}}$ is computed from the energy expression (73) rather than the field expression (71), so that $\mathbf{H}_{\mathrm{d,i}}$ can be interpreted as being the average value for the demagnetization field in cell i arising from a cell j having uniform magnetization $\mathbf{M}_j$.

It remains now to compute N_i. It follows from the magnetic reciprocity theorem [3] that N_i must be symmetric. (Reference [47] discusses also additional properties of N_i.) This means that the 3×3 matrix N_i holds only 6 independent entries,

$$N_i = \begin{bmatrix} N_{xx,i} & N_{xy,i} & N_{xz,i} \\ N_{xy,i} & N_{yy,i} & N_{yz,i} \\ N_{xz,i} & N_{yz,i} & N_{zz,i} \end{bmatrix}. \tag{76}$$

The entries, $N_{xx,i}$ etc., can be evaluated analytically [48, 47, 49]. First, define

$$f(x, y, z) = \frac{1}{2}y(z^2 - x^2)\sinh^{-1}\left(y/\sqrt{x^2 + z^2}\right)$$

$$+ \frac{1}{2}z(y^2 - x^2)\sinh^{-1}\left(z/\sqrt{x^2 + y^2}\right)$$

$$- xyz\arctan(yz/xR) + \frac{1}{6}(2x^2 - y^2 - z^2)R \tag{77}$$

$$g(x, y, z) = xyz\sinh^{-1}\left(z/\sqrt{x^2 + y^2}\right)$$

$$+ \frac{1}{6}y(3z^2 - y^2)\sinh^{-1}\left(x/\sqrt{y^2 + z^2}\right)$$

$$+ \frac{1}{6}x(3z^2 - x^2)\sinh^{-1}\left(y/\sqrt{x^2 + z^2}\right)$$

$$- \frac{1}{2}y^2 z\arctan(xz/yR) - \frac{1}{2}x^2 z\arctan(yz/xR)$$

$$- \frac{1}{6}z^3\arctan(xy/zR) - xyR/3, \tag{78}$$

where $R = \sqrt{x^2 + y^2 + z^2}$, and $\sinh^{-1}$ is the inverse hyperbolic sine, $\sinh^{-1}(x) = \log(x + \sqrt{1 + x^2})$. Note that the $f(x, y, z)$ and $g(x, y, z)$ are nothing else than the $F^{022}(x, y, z)$ and $F^{112}(x, y, z)$ defined in Appendix B, respectively. They describe magnetostatic interactions between parallel and perpendicular charged tiles, respectively. Then

$$4\pi\Delta_x\Delta_y\Delta_z N_{xx,i} =$$

$$8f(x_i, y_i, z_i) - 4\sum_{v \in A} f(v) + 2\sum_{v \in B} f(v) - \sum_{v \in C} f(v) \tag{79}$$

$$4\pi\Delta_x\Delta_y\Delta_z N_{xy}(x, y, z) =$$

$$8g(x_i, y_i, z_i) - 4\sum_{v \in A} g(v) + 2\sum_{v \in B} g(v) - \sum_{v \in C} g(v), \tag{80}$$

where A is the set of "nearest neighbors" to (x_i, y_i, z_i), B is the set of next nearest neighbors, and C is the set of corners of the 3×3 cube about (x_i, y_i, z_i):

$$A = \{(x_i \pm \Delta_x, y_i, z_i), (x_i, y_i \pm \Delta_y, z_i), (x_i, y_i, z_i \pm \Delta_z)\} \tag{81}$$

$$B = \{(x_i \pm \Delta_x, y_i \pm \Delta_y, z_i), (x_i \pm \Delta_x, y_i, z_i \pm \Delta_z),$$

$$(x_i, y_i \pm \Delta_y, z_i \pm \Delta_z)\} \tag{82}$$

$$C = \{(x_i \pm \Delta_x, y_i \pm \Delta_y, z_i \pm \Delta_z)\}, \tag{83}$$

so that $|A| = 6$, $|B| = 12$, and $|C| = 8$. The other four elements of N_i are computed analogously, by permuting x, y, z and Δ_x, Δ_y, Δ_z, with $N_{yy,i}$ and $N_{zz,i}$ using (79) and $N_{xz,i}$ and $N_{yz,i}$ using (80).

If we let ϕ represent the operator on f and g in the right hand side of (79) and (80), we see that $\phi/|V|^2$ is a second order discrete approximation to the differential operator $-\partial^6/\partial x^2\partial y^2\partial z^2$ [50]. If we define ψ_x/Δ_x^2 to be the second order discrete approximate to $-\partial^2/\partial^2 x$, $\psi_x(f)(x) = -f(x - \Delta_x, y, z) + 2f(x, y, z) - f(x + \Delta_x, y, z)$ (and likewise ψ_y and ψ_z), we see that ϕ can be

decomposed as $\psi_x \circ \psi_y \circ \psi_z$. This admits a relatively efficient approach to the evaluation of N_{xx} for the entire range of (x, y, z) of interest. First, evaluate f at each point on the mesh. Then, evaluate $\psi_z(f)$ at each point on the mesh, which can be done essentially in place. If there are n points in the mesh, evaluating $\psi_z(f)$ requires $2n$ subtractions. Then, evaluate ψ_y on the new values, and finally ψ_x, for a total of $6n$ subtractions (as compared to $26n$ additions/subtractions in a direct implementation of (79)). The other five terms of N_i can be evaluated using the same method.

As can be seen from (75), $\mathbf{H}_{\mathrm{d,i}}$ is a discrete (three dimensional) convolution of N_i with $\mathbf{M}_i$, so it can be computed efficiently using Fast Fourier Transform (FFT) techniques [51]. A few details of the application of the FFT in this case bear mentioning [52, 53].

The basics of the technique are to take the FFT of the N_i and $\mathbf{M}_i$ sequences, say $\tilde{N}_k$ and $\tilde{\mathbf{M}}_k$, multiply these together pointwise to obtain $\tilde{\mathbf{H}}_{\mathrm{d,k}}$, and then take the inverse FFT of $\tilde{\mathbf{H}}_{\mathrm{d,k}}$ to obtain $\mathbf{H}_{\mathrm{d,i}}$. Since the FFT and inverse FFT can be computed with operation count of $O(n \log n)$ (where n is the size of the set $\{i\}$), the computation of the entire set $\{\mathbf{H}_{\mathrm{d,i}}\}$ can be computed in $O(n \log n)$, as opposed to $O(n^2)$ resulting from a direct evaluation of (75).

However, the magnetization data in (75) should be interpreted as being finite in extent but lying in an infinite space. Since convolution-by-FFT produces a cyclic (periodic) convolution, the magnetization data need to be zero-padded to double length in each of the x, y, and z directions in order to remove wraparound artifacts. Note that this results in an eightfold increase in the number of points. The interaction coefficient sequence N_i also needs to be extended to this size, however it is not zero-padded but rather is extended through the origin into "negative" territory, where, following the usual FFT conventions, index $-i = (-i_x, -i_y, -i_z)$ is stored at the index corresponding to $(n_x - i_x, n_y - i_y, n_z - i_z)$.

Since the interaction coefficient sequence N_i is determined by the geometry of the problem, the FFT of this sequence, $\tilde{N}_k$, can be computed once during program initialization and saved for subsequent use. Moreover, the various symmetries of the N_{xx}, N_{xy}, ... terms [47], and the fact that these sequences are real (as opposed to complex), result in the transformed sequences $\tilde{N}_{xx,k}$, $\tilde{N}_{xy,k}$, ... having the same symmetries and also being purely real. As a result, only one octant of $\tilde{N}_k$ needs to be stored, and that storage can be as real (as opposed to complex) values.

The $\mathbf{M}_i$ sequence is also real; this property can be used to accelerate the FFT by almost a factor of two and reduce the storage requirements for $\tilde{\mathbf{M}}_k$ by half. ($\tilde{\mathbf{M}}_k$ is complex valued, but is conjugate symmetric with respect to the origin, so only one half-space needs to be stored.) The fact that large portions of the zero-padded $\mathbf{M}_i$ array are zero can also be used to significantly speed up the FFT.
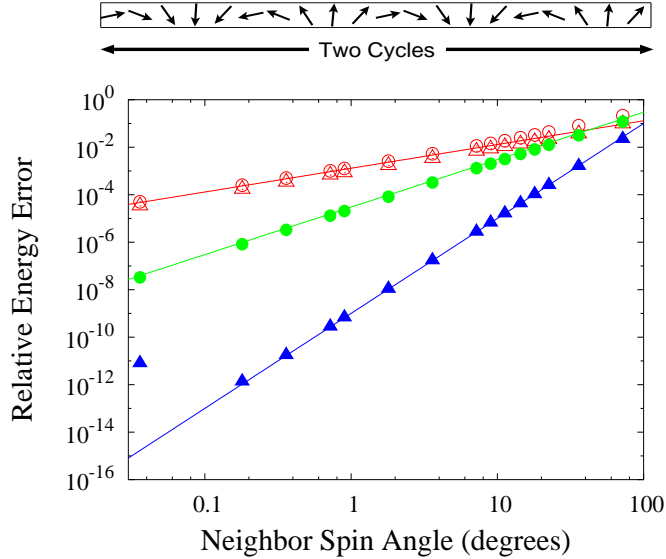
3.5 Boundary conditions

Fig. 9. One dimensional convergence study of exchange energy on an impressed magnetization spiral. Horizontal axis is the (constant) angle between neighboring spins, 720°/number of spins. Circles represent second order exchange method discussed in Sec. 3.3, triangles are a fourth order method presented in reference [32]. Open symbols (top line) are results using "free" boundary condition, $\partial \mathbf{m}/\partial \mathbf{n} = \mathbf{0}$; these show only first order convergence because the magnetization spiral does not obey this boundary condition. Closed symbols (bottom two lines) use the correct Dirichlet boundary conditions, and recover the quoted convergence rates, second and fourth order, respectively. The leftmost point on the lowest curve shows the limit of numeric accuracy imposed by round-off errors.

As discussed in Sec. 2.3 and 2.4, at grid points where the stencil for an expression extends beyond the boundaries of the part being simulated, the stencil will need to be adjusted. Typically this involves replacement of missing magnetization values (i.e., points corresponding to stencil values outside the part boundary) with relations involving boundary conditions and possibly additional points inside the part. These considerations apply not just to part boundaries, but across any interface where the magnetization fails to fulfill the smoothness requirements for the given expression. We consider in this subsection only the "free" boundary conditions arising in the case of no surface anisotropy. As discussed in Secs. 1 (equations (14)-(17)) and 2.4, other constraints are possible.

In general, boundary conditions may influence any of the energy terms. However, for the second order relations discussed here (Sec. 3), only the exchange energy is directly affected. Indeed, expressions (46) and (52) for the Zeeman term, expressions (55)-(58) for anisotropy, and (74) and (75) for demagnetization may be used unaltered at boundaries or in situations where $\mathbf{M}$ is discontinuous across cell faces.

However, examination of (64) reveals that that formula is undefined at boundaries; for example, if $\mathbf{r}_i$ is on the leftmost edge of the discretized mesh, then $\mathbf{r}_i - \Delta_x \hat{x}$ is outside the mesh, so we have no value for $\mathbf{m}$ there.

The most common solution to this problem is to introduce a "ghost" spin at the missing location, with value the same as the nearest spin inside the boundary, i.e., define $\mathbf{m}(\mathbf{r}_i - \Delta_x \hat{x}) = \mathbf{m}(\mathbf{r}_i)$. Here we implicitly assume that the boundary runs along the discretization cell surfaces, and is therefore exactly halfway between $\mathbf{r}_i - \Delta_x \hat{x}$ and $\mathbf{r}_i$. With this definition, the interpolated magnetization $\mathbf{m}(\mathbf{r})$ satisfies the usual Neumann boundary condition $\partial \mathbf{m}/\partial \mathbf{n} = \mathbf{0}$. This approach is sometimes referred to as using "mirror boundary conditions," because the magnetization is in some sense reflected across the boundary. It should be noted that this simple scheme for defining the value of the ghost spin only works for the second order method. The relations are more complicated when higher order methods are involved [32]. Also, the computed value for the field (65) at the edge spin $\mathbf{r}_i$ is only first-order accurate in Δ_x. However, the boundary region has narrow width Δ_x, so in the energy computation (64) a factor of Δ_x is introduced into the $|V_i|$ term; therefore the computed value for the total energy remains second order in Δ_x [32].

The usual artifact of applying an incorrect boundary condition is a loss in accuracy arising from a reduction in method order. This effect is shown in Fig. 9, where a uniform magnetization spiral is impressed upon a one dimensional rod. The magnetization pattern is not relaxed, but rather held fixed while the exchange energy is computed for different discretization scales. For this reason the usual "free" boundary conditions, $\partial \mathbf{m}/\partial \mathbf{n} = \mathbf{0}$, do not hold. To obtain full method accuracy it is necessary to apply the correct boundary conditions, which in this case are of the Dirichlet type.

4 Solving the LLG equation

When attempting to solve the LLG equation, accuracy needs to be preserved both in space and time. In order to look for time accuracy monitoring tools that might easily be implemented in a given code, let us first take the vector product of the right-hand side of the LLG equation (9) with $d\mathbf{m}/dt$. One gets

$$\mathbf{h}_{\text{eff}} \cdot \frac{d\mathbf{m}}{d\tau} = \alpha \left(\frac{d\mathbf{m}}{d\tau} \right)^2 \quad , \tag{84}$$

where, $\tau = \gamma_0 M_{\text{s}} t$, $\mathbf{m} = \mathbf{M}/M_{\text{s}}$, $\mathbf{h}_{\text{eff}} = \mathbf{H}_{\text{eff}}/M_{\text{s}}$. Equation (84) is local. Alternatively, starting from the general expression of the system's free energy

functional, its rate of change may, provided the applied field be time independent, be written as [3]

$$\frac{d \int \varepsilon_{\mathrm{T}}}{d\tau} = -\mu_0 M_{\mathrm{s}}^2 \int \left(\mathbf{h}_{\mathrm{eff}} \cdot \frac{d\mathbf{m}}{d\tau} \right) \quad . \tag{85}$$

There exists no local counterpart to this expression, due to the non-local nature of magnetostatic interactions. It follows from (84) and (85) that the damping parameter is related to the rate of change of the total free energy and the rate of change of the magnetization through

$$\alpha = -\frac{1}{\mu_0 M_{\mathrm{s}}^2} \left[\frac{\int d\varepsilon_{\mathrm{T}}/d\tau}{\int \left(d\mathbf{m}/d\tau \right)^2} \right] \quad . \tag{86}$$

As expected, the damping parameter may stay positive only if the overall energy decreases as time elapses. Two numerical equivalents to this important relation may be written down, namely

$$< \alpha > = \frac{\gamma_0 \Delta t}{\mu_0 M_{\mathrm{s}}} \left[\frac{-\sum_{\mathrm{i}=1}^{\mathrm{N}} \Delta \varepsilon_{\mathrm{i}}}{\sum_{\mathrm{i}=1}^{\mathrm{N}} \Delta \mathbf{m}_{\mathrm{i}}^2} \right] \quad , \tag{87}$$

where i is the node index, N the total node number, and the reduced time has been replaced by the physical time step in the calculation, and

$$\alpha_{\mathrm{MS}} = N \frac{\gamma_0 \Delta t}{\mu_0 M_{\mathrm{s}}} \left[\frac{-\sum_{\mathrm{i}=1}^{\mathrm{N}} \Delta \varepsilon_{\mathrm{i}}}{\left(\sum_{\mathrm{i}=1}^{\mathrm{N}} \Delta \mathbf{m}_{\mathrm{i}} \right)^2} \right] \quad , \tag{88}$$

which represents a transcription of (86) for the average magnetization, i.e. for the macro-spin equivalent to the magnetization distribution. Because of Schwartz' inequality, one always finds

$$\alpha_{\mathrm{MS}} \geq < \alpha > \quad . \tag{89}$$

This seemingly innocuous relation contains a deep meaning: any experiment which measures the time evolution of some average of the magnetization distribution is bound to yield a value larger than the true Gilbert damping parameter. On the other hand, it turns out that (87) provides an extremely sensitive tool when evaluating the accuracy of the numerical time integration of the LLG equation [54]. Note in passing that the variational form $\Delta \varepsilon_{\mathrm{i}} = -\mathbf{H}_{\mathrm{eff,i}} \cdot \Delta \mathbf{M}_{\mathrm{i}}$ provides the most accurate estimate of the energy change within the time step Δt.

A typical calculation of the kind is illustrated in Fig. 10 dealing with the effect of a spin-polarized current flowing through a sub-micron size elliptical element. Momentum transfer from the conduction electrons to the magnetization induces magnetization motion for large enough current densities and
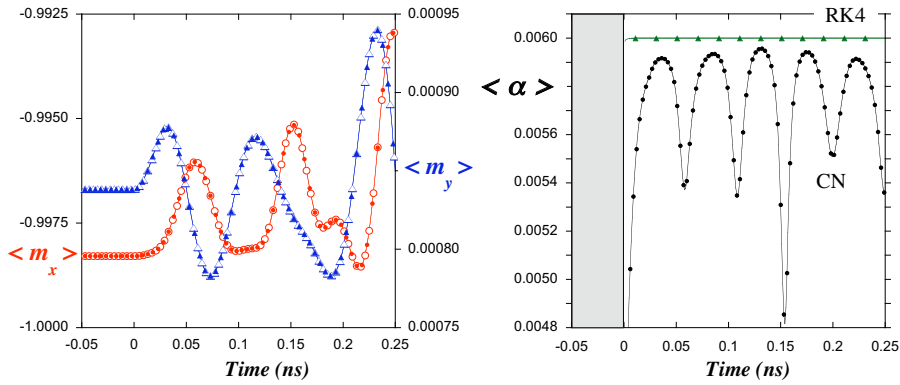
Fig. 10. Onset of magnetization motion under the influence of a spin-polarized current flowing across a sub-micron size elliptical element. The magnetization distribution at rest is stabilized by a field applied along the ellipse long axis and equal to $1.5H_K$, where H_K is the shape anisotropy field of the elliptical platelet. Current density: $J = 0.5$ A/μm^2 flowing from time $t = 0$ on. A tiny constant field (80 A/m or 1 Oe) is applied along the short ellipse axis, hence the non-zero value of the average m_y component prior to current application. Left: element-averaged magnetization components *vs* time along the long (m_x) and short (m_y) elliptical axes, respectively. Open symbols refer to the Crank-Nicholson solution with an implicit character restricted to exchange interactions; Full symbols refer to a 4th-order Runge-Kutta time integration. Right: volume-averaged damping parameter (Eq. 87) owing to the semi-implicit Crank-Nicholson (time step 12.5 fs) or explicit 4th-order Runge-Kutta (time step 25 fs) time integration schemes. Co-like materials parameters (Exchange constant: $A = 1.3 \times 10^{-11}$ J/m, saturation magnetization $M_s = 1500$ kA/m, damping coefficient $\alpha = 0.006$); Dimensions: 170 nm $\times$ 80 nm $\times$ 2.5 nm; One-layer-of-cells type simulation.

may lead to the existence of precessional states [55, 56, 57, 58, 59], [60] and loc. cit. Shortly after switching the current on, magnetization motion proves undistinguishable whether using a semi-implicit Crank-Nicholson integration scheme or the 4-th order explicit Runge-Kutta algorithm (Fig. 10-left). At longer times, however, magnetization trajectories would prove somewhat different. Energy dissipation, on the other hand, as monitored *via* Eq. 87, proves distinctively different (Fig. 10-right) for the two time integration schemes. The Runge-Kutta algorithm leads to a numerical damping parameter equal to the nominal value in this calculation to a better than 10^{-6} relative accuracy for the 25 fs time step considered. Rather large fluctuations in the numerical damping parameter $< \alpha >$ are seen to arise from the implicit integration scheme in spite of its unconditional stability. Generally speaking, $< \alpha >$ is seen to be significantly depressed whenever the magnetization becomes stationary, a result ascribed to residual numerical noise in the solution of a large set of linear equations (sparse matrix) by means of iterative methods. Such

considerations become particularly important when dealing with long time integrations such as requested in spin transfer problems.

5 Comparing methods

Numerical methods outlined in sections 2 and 3 do differ in the order of approximations for exchange interactions and boundary conditions. More significantly, perhaps, they differ in the evaluation of the demagnetizing field, direct evaluation at nodes in the first case, field averaged over the cell volume in the second. The approach described in section 3 uses constant magnetization cells, i.e., zero order expansion for the magnetization $\mathbf{m(r)}$. Note, however, that cell averaging, or indeed more complex integration approaches, may equally be applied to cells with a constant divergence (1st order expansion for the magnetization). The real question that arises from the different modeling options is the degree of coherence in approximation levels. Magnetization dynamics raises an additional issue, namely, is there a best numerical implementation for the LLG equation? In other words, should a mapping of the magnetization and the effective field onto the nodes of a regular mesh be preferred to motion involving a cell-averaged magnetization and a cell-averaged field, or *vice-versa*? The point being that in general, $\langle \mathbf{m}(t) \times \mathbf{H}_{\mathrm{eff}}(t) \rangle \neq \langle \mathbf{m}(t) \rangle \times \langle \mathbf{H}_{\mathrm{eff}}(t) \rangle$. We do not provide general answers to these questions in the following but, rather, analyze the convergence proper to each approach when dealing with the reversal of a rectangular platelet under the action of a slightly off-axis magnetic field applied at time $t = 0$. The specifics of the test problem considered here, which is the second part of μMAG Problem No. 4 [61], are shown in Fig. 11. At time $t = 0$ a uniform field is applied in-plane at $190°$ counterclockwise from the positive x-axis. The applied field causes the spins in the middle portion of the sample to rotate clockwise, and the spins on either end to rotate counterclockwise. The differing rotation directions results from the relative angle of the applied field with respect to the initial position of the spins in the middle of the plate in contrast to the spins at the ends, but the origin of the motion is perhaps not immediately obvious. The damping parameter α is relatively small, so the spin evolution is dominated by precessional motion. In the middle part of the sample, $\mathbf{H} \times \mathbf{m}$ is directed upward $(+z)$, so the initial motion of the spins in the middle is up and out of the film plane. In response, a large opposing demagnetization field is generated directed into the film plane $(-z)$. Precession about this demagnetizing field results in the clockwise rotation of these spins, as seen in Fig. 11(b). At the ends, the initial spin motion is in the $-z$ direction, the resulting demagnetizing field points along $+z$, and so the rotation of the spins at either end is counterclockwise.

After approximately 0.16 ns, the respective rotations generate two $360°$-character domain walls, one on either end (Fig. 11(c)), which are gradually pushed off the sample as the center domain expands (Fig. 11(d)). As the walls are forced off the ends, the confined geometry leads to very tight magnetization
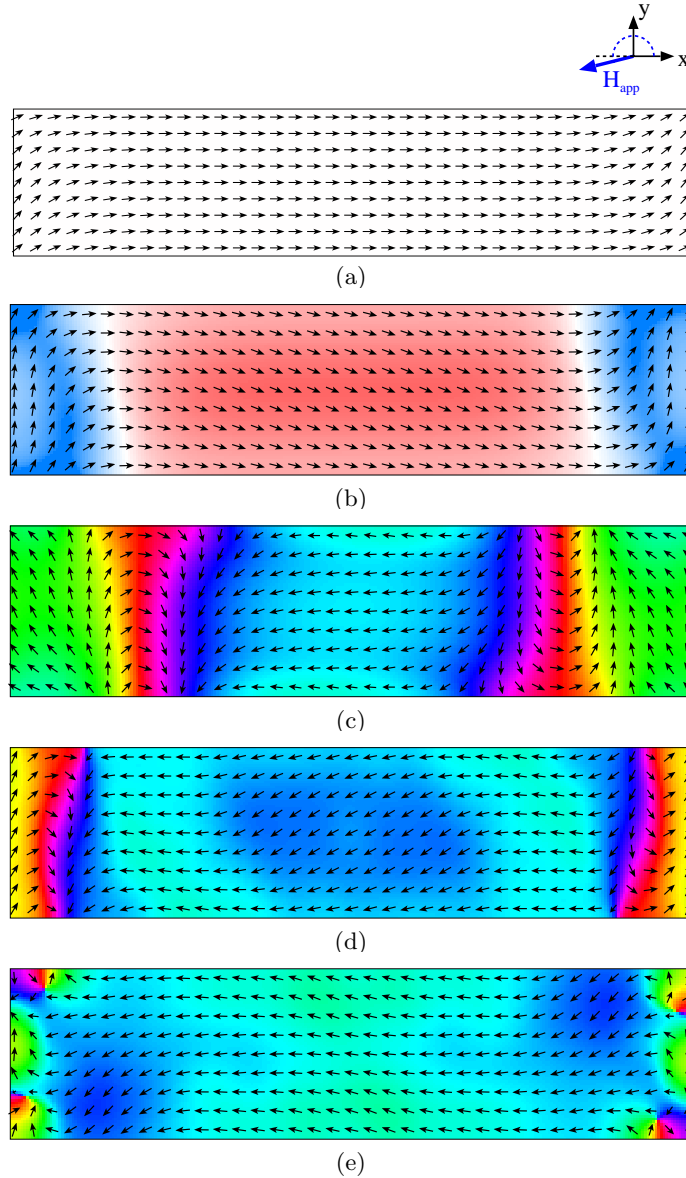
Fig. 11. Magnetization states for μMAG Problem 4b [61]. Sample is a $Ni_{80}Fe_{20}$ slab with dimensions 500 nm $\times$ 125 nm $\times$ 3 nm, material parameters A=13 pJ/m, M_s=800 kA/m, K=0 J/m^3, $\alpha = 0.02$, $\gamma_0 = 2.211 \times 10^5$ m/A·s. Dynamic simulation, starting in a zero-field equilibrium "S"-state (a). At time $t = 0$ fs a uniform applied field, $\mu_0 \mathbf{H}_{app} = (-35.5, -6.3, 0)$ mT, is instantaneously applied. By 60 fs (b), domain rotation has begun. Large angle ($\approx 360°$) domain walls are formed by 160 fs (c), which are slowly pushed outwards (450 fs, (d)) and off the ends by 520 fs (e). In (b), the color indicates the z-component of the magnetization: red is +z (out of the page), blue is -z (into the page). In (c)-(e), color indicates in-plane magnetization angle. These images taken from a simulation using the energy-based method, with $255 \times 63 \times 1$ cell count.

(a)   (b)
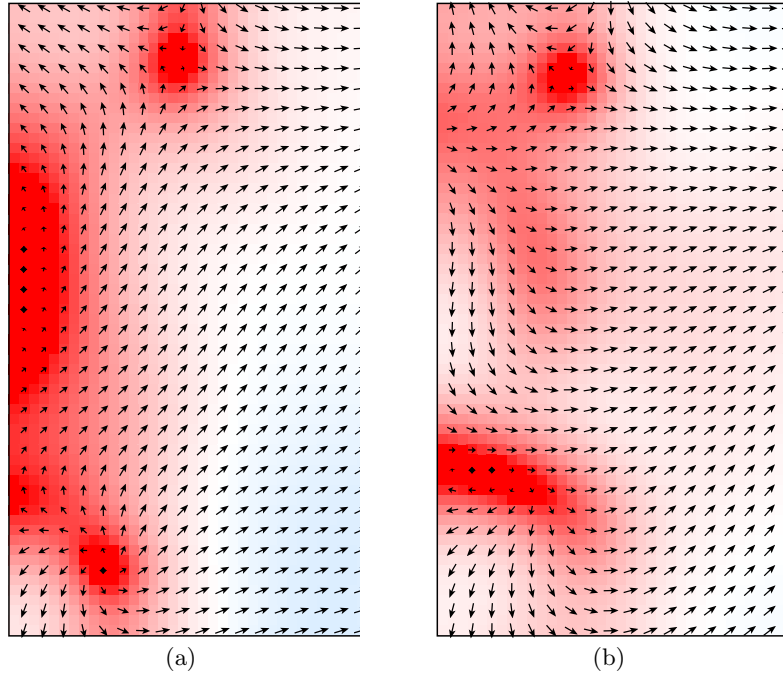
Fig. 12. Details at left edge of simulation in Fig. 11, at times $t = 500$ fs (a) and $t = 520$ fs (b). Cross-tie (or anti-vortex) at top and distorted vortex at bottom form from ends of $360°$ wall. The half-vortex visible in the middle of the left edge in (a) is a remanent of the $360°$ wall, which is pushed off the edge by 520 fs (b) as the cross-tie and distorted vortex move inward. Color indicates the z-component of the magnetization, with red for $m_z > 0$ (i.e., out of the page), blue for $m_z < 0$, and white for $m_z \approx 0$.

structures containing vortices and cross-ties (also called anti-vortices), which require a very fine mesh to properly resolve (Figs. 11(e-f), 12).

These effects are reflected in the simulation results displayed in Figs. 13 and 14. The simulations all agree fairly well until some time after 0.4 ns, corresponding to the annihilation of the $360°$ domain walls. After that, although the features described in Figs. 11 and 12 prove qualitatively similar in all simulations, discretization effects are clearly evident, especially in the field-based simulations shown in Fig. 13. In this figure, the single-layer simulations do not appear to be converging towards the same limit as the three-layer simulations, although the 127x31x1 solution proves rather close to the converged 500x125x3 energy-based solution (see Fig. 15). Whether or not this result is purely coincidental is hard to say. We note, however, that the most compact set of initial $\langle \mathbf{m}_y \rangle$ values including both approaches is obtained for the ex-
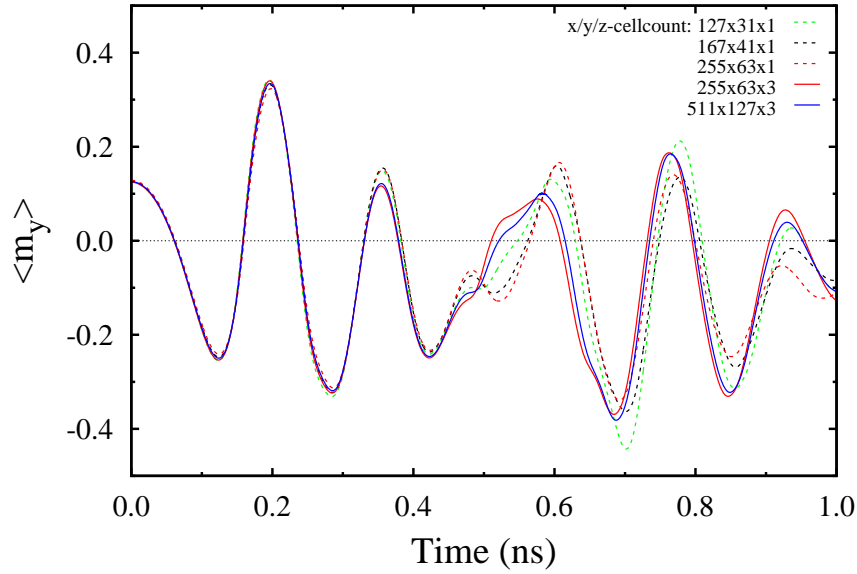
Fig. 13. Average m_y versus time results for test problem from Fig. 11 using field-based method of Sec. 2, with different x/y/z cell counts as indicated. In-plane counts 127×31 yields ≈ 4 nm square cells, $167 \times 41 \approx 3$ nm square cells, $255 \times 63 \approx 2$ nm square cells. Single-layer simulations (z cell count=1) appear to converge towards a different limit than the multi-layer simulations (z cell count=3).

treme meshing conditions, with $\langle \mathbf{m}_y \rangle = 0.12472109$ (field-based), 0.12526786 (energy-based) for the 127x31x1 discretization, 0.12567210 (field-based) and 0.12599484 (energy-based) for the ≈ 1 nm cubic mesh size. The larger variability in initial conditions in the field approach is undoubtedly responsible in part for the sizeable differences in time integration observed at later times and it is not even certain that three layers suffice for full convergence. In contrast, the results from the energy-based approach shown in Fig. 14 do in this test manifest only minor z-layer discretization effects, and appear to converge in a relatively straightforward manner. As noted above, this is probably due more to the effect of using a cell-averaged demagnetizing field as opposed to any intrinsic property of the energy-based approach, and presumably indicates that the mid-plane (mid-cell) demagnetizing field samples are not generally truly representative of the field profile through the thickness of the film (cell), an effect alluded to earlier.

   The important point from this comparison, as seen in Fig. 15, is that both methods converge towards similar limits, and either way a very small cell size is required to approach that limit. It must be stressed that the cell size required here, ≈ 1 nm, is much smaller than the exchange length for this ma-
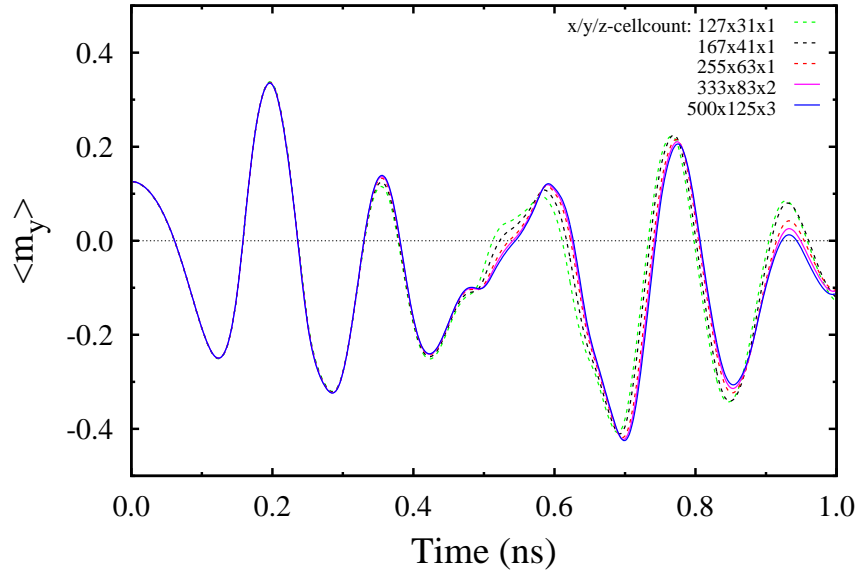
Fig. 14. Average m_y versus time results for test problem from Fig. 11 using energy-based method of Sec. 3, with various x/y/z cell counts as indicated. Single-layer and multi-layer simulations converge to same limit. Single-layer $500 \times 125 \times 1$ results (not shown) are indistinguishable from multi-layer $500 \times 125 \times 3$ results.

terial, which by (5) is about 5.7 nm. This illustrates the importance of always checking for discretization effects in micromagnetic simulations, especially in confined geometries with small magnetic structures such as vortices and cross-ties. We note in closing that a subtle influence of the approximation order in the exchange interactions and boundary conditions may not at this stage be ruled out.

6 Conclusion

This short review of finite difference methods applied to micromagnetics provides the reader with all the necessary ingredients to develop his or her own code. Different approximations have been discussed for exchange interactions and boundary conditions. Ways to include general boundary conditions have also been indicated. The appendices provide all required integrals for the definition of magnetostatic interaction coefficients owing to one's own choice regarding discretization. Provided care is taken in the choice of a proper meshing and time integration step, the field- or energy-based methods described above lead to comparable meshing sensitivity as evidenced in Fig. 15. On
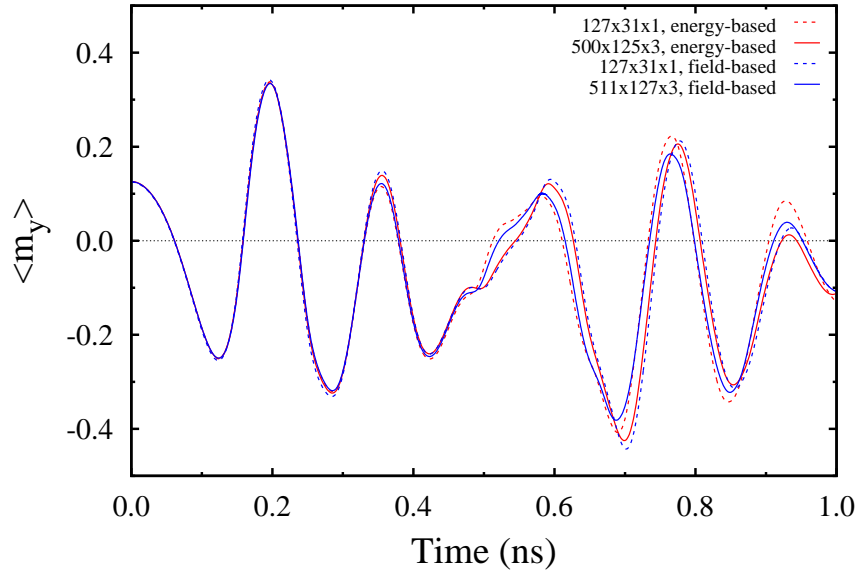
Fig. 15. Test problem results comparing field-based (blue curves) and energy-based (red curves) approaches. Cell count $500 \times 125 \times 3$ corresponds to discretizing with 1 nm cubes.

the whole, numerical micromagnetics relying on finite difference methods has reached a high maturity level. As already stated, however, available data do not show convergence towards a single $\langle \mathbf{m}_y \rangle(t)$ trajectory for this particular problem. Lastly, if finite difference methods prove extremely efficient in terms of computation time due to an extensive use of Fast Fourier Transforms, they display excessive discretization artifacts when dealing with curved geometries. Although that dependence needs to be quantified more precisely, work continues on the issue, and practical solutions are expected in the near future.

A Demagnetizing field : useful integrals

For parallelepipedic volume cells and rectangular surface tiles, defining $\rho = \sqrt{(u^2 + v^2 + w^2)}$, $L_u = \frac{1}{2}ln(\frac{\rho+u}{\rho-u})$, $P_u = \arctan(\frac{vw}{u\rho})$, and L_v, L_w, P_v, P_w through permutation in the variables u, v, w, all interaction coefficients allowing for a direct evaluation of the demagnetizing field at any position in space (except corners) may be evaluated with the help of the following integrals [62]:

$$H_u^{111} = \int \int \int \frac{u}{\rho^3} du dv dw = +uP_u - vL_w - wL_v$$

$$H_v^{111} = \int \int \int \frac{v}{\rho^3} du dv dw = +vP_v - wL_u - uL_w$$

$$H_w^{111} = \int \int \int \frac{w}{\rho^3} du dv dw = +wP_w - uL_v - vL_u$$

$$H_u^{110} = \int \int \frac{u}{\rho^3} du dv = -L_v$$

$$H_v^{110} = \int \int \frac{v}{\rho^3} du dv = -L_u$$

$$H_w^{110} = \int \int \frac{w}{\rho^3} du dv = +P_w$$

$$(90)$$

$$H_u^{011} = \int \int \frac{u}{\rho^3} dv dw = +P_u$$

$$H_v^{011} = \int \int \frac{v}{\rho^3} dv dw = -L_w$$

$$H_w^{011} = \int \int \frac{w}{\rho^3} dv dw = -L_v$$

$$H_u^{101} = \int \int \frac{u}{\rho^3} du dw = -L_w$$

$$H_v^{101} = \int \int \frac{v}{\rho^3} du dw = +P_v$$

$$H_w^{101} = \int \int \frac{w}{\rho^3} du dw = -L_u \quad .$$

B Potential : useful integrals

Defining $\rho = \sqrt{(u^2 + v^2 + w^2)}$, $L_u = \frac{1}{2}ln(\frac{\rho+u}{\rho-u})$, $Q_u = u\arctan(\frac{vw}{u\rho})$, and L_v, L_w, Q_v, Q_w through permutation in the variables u, v, w, the necessary

integrals for the computation of the cell- or tile-averaged scalar potential list as follows [62]:

$$F^{220} = \frac{1}{2}u(v^2 - w^2)L_{\mathrm{u}} + \frac{1}{2}v(u^2 - w^2)L_{\mathrm{v}} - uvQ_{\mathrm{w}} + \frac{1}{6}\rho(2w^2 - u^2 - v^2)$$

$$F^{202} = \frac{1}{2}w(u^2 - v^2)L_{\mathrm{w}} + \frac{1}{2}u(w^2 - v^2)L_{\mathrm{u}} - wuQ_{\mathrm{v}} + \frac{1}{6}\rho(2v^2 - w^2 - u^2)$$

$$F^{022} = \frac{1}{2}v(w^2 - u^2)L_{\mathrm{v}} + \frac{1}{2}w(v^2 - u^2)L_{\mathrm{w}} - vwQ_{\mathrm{u}} + \frac{1}{6}\rho(2u^2 - v^2 - w^2)$$

$$F^{211} = uvwL_{\mathrm{u}} + \frac{1}{6}w(3u^2 - w^2)L_{\mathrm{v}} + \frac{1}{6}v(3u^2 - v^2)L_{\mathrm{w}} -$$
$$\frac{1}{6}u(uQ_{\mathrm{u}} + 3vQ_{\mathrm{v}} + 3wQ_{\mathrm{w}}) - \frac{1}{3}\rho vw$$

$$F^{112} = uvwL_{\mathrm{w}} + \frac{1}{6}v(3w^2 - v^2)L_{\mathrm{u}} + \frac{1}{6}u(3w^2 - u^2)L_{\mathrm{v}} -$$
$$\frac{1}{6}w(wQ_{\mathrm{w}} + 3uQ_{\mathrm{u}} + 3vQ_{\mathrm{v}}) - \frac{1}{3}\rho uv$$

$$F^{121} = uvwL_{\mathrm{v}} + \frac{1}{6}u(3v^2 - u^2)L_{\mathrm{w}} + \frac{1}{6}w(3v^2 - w^2)L_{\mathrm{u}} -$$
$$\frac{1}{6}v(vQ_{\mathrm{v}} + 3wQ_{\mathrm{w}} + 3uQ_{\mathrm{u}}) - \frac{1}{3}\rho wu$$

$$F^{221} = \frac{1}{6}uw(3v^2 - w^2)L_{\mathrm{u}} + \frac{1}{6}vw(3u^2 - w^2)L_{\mathrm{v}} +$$
$$\frac{1}{24}(6u^2v^2 - u^4 - v^4)L_{\mathrm{w}} - \frac{1}{6}uv(uQ_{\mathrm{u}} + vQ_{\mathrm{v}} + 3wQ_{\mathrm{w}}) + \frac{1}{24}\rho(2w^3 - 3w(u^2 + v^2))$$

$$F^{212} = \frac{1}{6}wv(3u^2 - v^2)L_{\mathrm{w}} + \frac{1}{6}uv(3w^2 - v^2)L_{\mathrm{u}} +$$
$$\frac{1}{24}(6w^2u^2 - w^4 - u^4)L_{\mathrm{v}} - \frac{1}{6}wu(wQ_{\mathrm{w}} + uQ_{\mathrm{u}} + 3vQ_{\mathrm{v}}) + \frac{1}{24}\rho(2v^3 - 3v(w^2 + u^2))$$

$$F^{122} = \frac{1}{6}vu(3w^2 - u^2)L_{\mathrm{v}} + \frac{1}{6}wu(3v^2 - u^2)L_{\mathrm{w}} +$$
$$\frac{1}{24}(6v^2w^2 - v^4 - w^4)L_{\mathrm{u}} - \frac{1}{6}vw(vQ_{\mathrm{v}} + wQ_{\mathrm{w}} + 3uQ_{\mathrm{u}}) + \frac{1}{24}\rho(2u^3 - 3u(v^2 + w^2))$$

$$F^{222} = \frac{1}{24}u(6v^2w^2 - v^4 - w^4)L_{\mathrm{u}} +$$
$$\frac{1}{24}v(6w^2u^2 - w^4 - u^4)L_{\mathrm{v}} +$$
$$\frac{1}{24}w(6u^2v^2 - u^4 - v^4)L_{\mathrm{w}} -$$
$$\frac{1}{6}uvw(uQ_{\mathrm{u}} + vQ_{\mathrm{v}} + wQ_{\mathrm{w}}) + \frac{1}{60}\rho(u^4 + v^4 + w^4 - 3(u^2v^2 + v^2w^2 + w^2u^2)) \quad .$$

$$(91)$$

All of these integrals are equal to their counterparts in [6]. The F^{200} integral in [6] proves, however, erroneous; it should read: $F^{200} = uL_{\mathrm{u}} - \rho$.

References

1. A. E. LaBonte, "Two-Dimensional Bloch-Type Domain Walls in Ferromagnetic Films," J. Appl. Phys. **40**, 2450 (1969).
2. R. Hertel, O. Fruchart, S. Cherifi, P. -O. Jubert, S. Heun, A. Locatelli, J. Kirschner, "Three-dimensional magnetic flux-closure patterns in mesoscopic Fe islands, " Phys. Rev. B **72**, 214409 (2005).
3. W.F. Brown: *Micromagnetics* (Interscience Publishers, 1963).
4. J. Miltat *Domains and Domain Walls in Soft Magnetic Materials, Mostly* in *Applied Magnetism*, ed. by R. Gerber, *et al.* (Kluwer, Dordrecht, 1994) p. 221-308.
5. A. Aharoni: *Introduction to the Theory of Ferromagnetism* (Oxford, 1996).
6. A. Hubert, R. Schäfer: *Magnetic Domains* (Springer-Verlag, Berlin, 1998).
7. H. Kronmüller, M. Fähnle: *Micromagnetism and the Microstructure of Ferromagnetic Solids* (Cambridge University Press, 2003)
8. H. Kronmüller, this volume.
9. C. Kittel, "Physical theory of ferromagnetic domains," Rev. Mod. Phys., **21**, 541–583 (1949).
10. J. C. S. Kools, Th. G. S. M. Rijks, A. E. M. De Veirman and R. Coehoorn, "On the ferromagnetic interlayer coupling in exchange-biased spin-valve multilayers," IEEE Trans. Magn., **31**, 3918–3920 (1995).
11. D. Wei and H. N. Bertram, "Interlayer coupling and surface roughness in GMR spin valves," IEEE Trans. Magn., **32**, 3434–3436 (1996).
12. T. L. Gilbert, "A Lagrangian formulation of the gyromagnetic equation of the magnetization field," Phys. Rev. **100**, 1243 (1955); T. L. Gilbert: "Formulation, Foundations and Applications of the Phenomenological Theory of Ferromagnetism", Ph-D thesis, Illinois Institute of Technology, Chicago (1956); T. L. Gilbert, "A Phenomenological Theory of Damping in Ferromagnetic Materials," IEEE Trans. Magn., **40**, 3443–3449 (2004).
13. M. Labrune and J. Miltat, "Wall structures in ferro/antiferromagnetic exchange-coupled bilayers: A numerical micromagnetic approach," J. Magn. Magn. Mat., **151**, 231–245 (1995).
14. G. T. Rado and J. R. Weertman, "Spin-wave resonance in a ferromagnetic metal," J. Phys. Chem. Solids, **11**, 315–333 (1959).
15. K. Yu. Guslienko and A. N. Slavin, "Boundary conditions for magnetization in magnetic nanoelements," Phys. Rev. B, **72**, 014463 (2005).
16. G. J. Parker, C. Cerjan, and D. W. Hewett, "Embedded curve boundary method for micromagnetic simulations," J. Magn. Magn. Mat., **214**, 130–138 (2000).
17. D. G. Porter and M. J. Donahue, "Generalization of a two-dimensional micromagnetic model to non-uniform thickness," J. Appl. Phys., **89**, 7257–7259 (2001).
18. C.J. García-Cervera, Z. Gimbutas, and Weinan E, "Accurate numerical methods for micromagnetics simulations with general geometries," J. Comp. Physics, **184**, 37–52 (2003).

19. G. Albuquerque: "Magnetization Precession in Confined Geometry: Physical and Numerical Aspects", Ph-D Thesis (in English), Paris-Sud University, Orsay (2002).

    http://tel.ccsd.cnrs.fr/documents/archives0/00/00/21/75/

20. J.-C. Toussaint, A. Marty, N. Vukadinovic, J. B. Youssef, and M. Labrune, "A new technique for ferromagnetic resonance calculations," Computational Materials Science, **24**, 175–180 (2002).

21. J. Eastwood, R. Hockney and D. Lawrence, "P3M3DP—The 3-dimensional periodic particle-particle-particle-mesh program," Comput. Phys. Commum., **19**, 215–261 (1980).

22. R. Hockney and J. Eastwood: *Computer Simulation using Particles* (McGraw-Hill, New York, 1981).

23. S. W. Yuan and H. N. Bertram, "Fast adaptive algorithms for micromagnetics," IEEE Trans. Magn., **28**, 2031–2036 (1992).

24. D. V. Berkov, K. Ramstöck and A. Hubert, "Solving micromagnetic problems—towards an optimal numerical-method," Phys. Stat. Sol. (a), **137**, 207–225 (1993).

25. K. Ramstöck, T. Leibl and A. Hubert, "Optimizing stray field computations in finite-element micromagnetics," J. Magn. Magn. Mat., **135**, 97–110 (1994).

26. W. H. Press, S. A. Teukolsky, W. T. Wetterling, B. P. Flannery: *Numerical Recipes in Fortran 77: The Art of Scientific Computing* (Cambridge University Press, 2001).

27. S. Shtrickman and D. Treves, "On the Resolution of Brown's Paradox," J. Appl. Phys., **31**, S72–S73 (1960).

28. W. Rave, K. Ramstöck, and A. Hubert, "Corners and nucleation in micromagnetics," J. Magn. Magn. Mat., **183**, 329–333 (1998).

29. A. Thiaville, D. Tomáš, and J. Miltat, "On corner singularities in micromagnetics," Phys. Stat. Sol. (a), **170**, 125–135 (1998).

30. P. Trouilloud and J. Miltat, "Néel lines in ferrimagnetic garnet epilayers with orthorhombic anisotropy and canted magnetization," J. Magn. Magn. Mat., **66**, 194–212 (1987).

31. J. Miltat, A. Thiaville, and P. Trouilloud, "Néel lines structures and energies in uniaxial ferromagnets with quality factor $Q > 1$," J. Magn. Magn. Mat., **82**, 297–308 (1989).

32. M. J. Donahue and D. G. Porter, "Exchange energy formulations for 3D micromagnetics," Physica B, **343**, 177–183 (2004).

33. S. W. Yuan, H. N. Bertram, J. F. Smyth, and S. Schultz, "Size effects of switching fields of thin Permalloy particles," IEEE Trans. Magn., **28**, 3171–3173 (1992).

34. Y. Zheng and J.-G. Zhu, "Switching field variation in patterned submicron magnetic film elements," J. Appl. Phys., **81**, 5471-5473 (1997).

35. W. Rave and A. Hubert, "Magnetic ground state of a thin-film element," IEEE Trans. Magn., **36**, 3886–3899 (2000).

36. J. Miltat, G. Albuquerque and A. Thiaville, "An introduction to micromagnetics in the dynamic regime" : in B. Hillebrands and A. Thiaville (Eds,): *Spin Dynamics in Confined Magnetic Structures I*, (Springer Verlag Berlin Heidelberg 2001) pp. 1–33.

37. R. Hertel, "Thickness dependence of magnetization structures in thin Permalloy rectangles," Z. Metallkd. **93**, 957–962 (2002)

38. W. Rave, K. Fabian and A. Hubert, "Magnetic states of small cubic particles with uniaxial anisotropy," J. Magn. Magn. Mat., **190**, 332–348 (1998).

39. M. J. Donahue, D. G. Porter, R. D. McMichael, and J. Eicke, "Behavior of muMAG Standard Problem No. 2 in the small particle limit," J. Appl. Phys., **87**, 5520–5522 (2000).

40. P. J. Davis and P. Rabinowitz: *Methods of Numerical Integration* (Academic Press, Orlando, 1984).

41. J. Stoer and R. Bulirsch: *Introduction to Numerical Analysis* (Springer-Verlag, New York, 1993).

42. A. Moschel, A. Zangwill, and M. Stiles, "Simulations of inhomogeneous magnetization processes in ultrathin films with growth-induced roughness," J. Appl. Phys., **79**, 4994–4994 (1996).

43. M. J. Donahue and R. D. McMichael, "Exchange energy representations in computational micromagnetics," Physica B, **233**, 272–278 (1997).

44. A. Thiaville, J. M. Garciá, R. Dittrich, J. Miltat, and T. Schrefl, "Micromagnetic study of Bloch-point-mediated vortex core reversal," Phys. Rev. B, **67**, 094410 (2003).

45. M. J. Donahue, "A variational approach to exchange energy calculations in micromagnetics," J. Appl. Phys., **83**, 6491–6493 (1998).

46. M. J. Donahue and D. G. Porter: "OOMMF User's Guide, Version 1.0," Interagency Report NISTIR 6376, National Institute of Standards and Technology, Gaithersburg, MD (Sept 1999).

47. A. J. Newell, W. Williams, and D. J. Dunlop, "A generalization of the demagnetizing tensor for nonuniform magnetization," Journal of Geophysical Research-Solid Earth, **98** 9551–9555 (1993).

48. M. E. Schabes and A. Aharoni, "Magnetostatic interaction fields for a 3-dimensional array of ferromagnetic cubes," IEEE Trans. Magn., **23**, 3882–3888 (1987).

49. H. Fukushima, Y. Nakatani, and N. Hayashi, "Volume average demagnetizing tensor of rectangular prisms," IEEE Trans. Magn., **34** 193–198 (1998).

50. M. Abramowitz and I.A. Stegun (Eds.): *Handbook of Mathematical Functions* (U.S. NBS, Washington D.C., 1970).

51. T. G. Stockham, "High Speed Convolution and Correlation," Joint Computer Conference Proceedings, **28**, 229–233 (1966).

52. D. Donnelly and B. Rust, "The Fast Fourier Transform for Experimentalists, Part I: Concepts," Computing in Science and Engineering, **7** (2), 80–88 (2005).

53. D. Donnelly and B. Rust, "The Fast Fourier Transform for Experimentalists, Part II: Convolutions," Computing in Science and Engineering, **7** (4), 92–95 (2005).

54. G. Albuquerque, J. Miltat, and A. Thiaville, "Self-consistency based control scheme for magnetization dynamics," J. Appl. Phys., **89**, 6719–6721 (2001).

55. J. C. Slonczewski, "Current-driven excitation of magnetic multilayers," J. Magn. Magn. Mat., **159**, L1–L7 (1996).

56. J. Z. Sun, "Spin-current interaction with a monodomain magnetic body: A model study," Phys. Rev. B, **62**, 570–578 (2000).

57. J. Miltat, G. Albuquerque, A. Thiaville, and C. Vouille, "Spin transfer into an inhomogeneous magnetization distribution," J. Appl. Phys., **89**, 6982–6984 (2001).

58. M. D. Stiles, J. Xiao, and A. Zangwill, "Phenomenological theory of current-induced magnetization precession," Phys. Rev. B, **69**, 054408 (2004).

59. M. D. Stiles: this volume.
60. M. D. Stiles and J. Miltat, "Spin-transfer torque and dynamics" : in B. Hillebrands and A. Thiaville (Eds,): *Spin Dynamics in Confined Magnetic Structures III*, (Springer Verlag Berlin Heidelberg 2006) pp. 225-308.
61. Micromagnetic Modeling Activity Group (μMAG) at the National Institute of Standards and Technology, Gaithersburg, Maryland:

    `http://www.ctcms.nist.gov/~rdm/mumag.org.html`

62. D. Tomáš: "Modelling of Micromagnetic Structures", Ph-D Thesis (in English), Paris-Sud University, Orsay and Charles University, Prague (1999).

Index